Engineering Structures 289 (2023) 116281

Contents lists available at ScienceDirect

Engineering Structures

journal homepage: www.elsevier.com/locate/engstruct

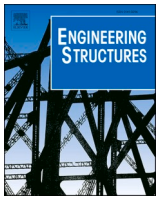

A hybrid inter-module connection for steel modular building systems with SMA and high-damping rubber components

Dan-Adrian Corfar, Konstantinos Daniel Tsavdaridis *

Department of Engineering, School of Science & Technology, City, University of London, Northampton Square, EC1V 0HB London, UK

ARTICLE INFO

Keywords:
Design for deconstruction
Design for reuse
High-damping rubber
Inter-module connections
Shape-memory alloys
Steel modular building systems

ABSTRACT

The recent technological advancements achieved in modular construction have accelerated the trend of building taller self-standing steel modular building systems (MBSs), leading to a consensus among researchers regarding the vital role that inter-module connections (IMCs) play in the structural performance of MBSs subjected to extreme lateral loading. However, existing IMCs are typically designed such that the global structural system heavily relies on the hysteresis of the steel framing members, leading to severe sustained damage and costly, impractical retrofitting programmes. To unlock the full "disassembly and reuse" potential of steel MBSs, IMCs can be designed to contribute more effectively to the global damage distribution mechanism, by engaging specific "fuse" components which are easy to replace, improving the reuse prospects of volumetric modules. In this regard, the present study proposes a novel, hybrid IMC using custom corner fittings, a high-damping rubber (HDR) core and a shape-memory alloy (SMA) bolt. Calibrated and validated material models using data from experimental material characterisation tests have facilitated the full characterisation of the hybrid mechanical response, determining the deformation modes, stress states, hysteresis loops and mechanical parameters. The parametric FEA included the variation of bolt preload, endplate thickness, axial load magnitude and the vertical layout of the HDR core. The study represents a preliminary, proof-of-concept investigation, showcasing the favourable cyclic performance of the proposed IMC under the main deformation modes expected in tall self-standing MBSs during lateral loading. Due to the effective contribution of each component to the combined hybrid response, the connection succeeds in preventing the formation of significant plastic damage in the MBS's corner fittings to facilitate reusability of modules.

1. Introduction

Modular Building Systems (MBSs) are a sub-category of Modular Construction referring to the highest level of prefabrication [1], in which entire pre-engineered volumetric frames are manufactured within tight tolerance levels in a controlled factory environment, delivered to the location of the project on a 'just-in-time' basis, and finally assembled into complete building systems. The recent technological advancements achieved in Off-Site Manufacturing (OSM), Off-Site Construction (OSC) and Building Information Modelling (BIM) have accelerated the expansion of MBSs within the high-rise construction sector. Corner-supported volumetric modules made of hot-rolled structural steel or steel–concrete composite frame members [2] are a common structural solution in high-rise MBSs due to high strength-to-weight ratio, high load-carrying capacity, and enhanced overall sustainability [3] and represent the scope of this study.

1.1. The role of inter-module connections in the structural response of steel MBSs

The discrete nature of vertical and horizontal diaphragms made of volumetric modules connected through their corners at each level poses a challenge for the resistance and stability of high-rise steel MBSs under earthquake and strong wind scenarios as the increased height amplifies the effects of lateral loads. In this regard, tremendous effort has been demonstrated among researchers and academics to acquire a deeper understanding of the role that inter-module connections (IMCs) play in the structural response of steel MBSs under the action of lateral loading. Annan et al. [4] investigated the effect of reversed-cyclic loading on the hysteretic responses of a conventional braced steel frame and a steel MBS braced frame, and attributed the different load transfer mechanisms to the presence of vertical inter-module connections (IMCs) between floor and ceiling beams in the steel MBS frame. Fathieh and

* Corresponding author.
E-mail address: Konstantinos.tsavdaridis@city.ac.uk (K.D. Tsavdaridis).

https://doi.org/10.1016/j.engstruct.2023.116281
Received 16 January 2023; Received in revised form 4 April 2023; Accepted 3 May 2023
Available online 16 May 2023

Mercan [5] assessed the seismic demand and capacity of steel MBSs by performing nonlinear static pushover and incremental dynamic analyses (IDA) on a detailed OpenSees® 4-storey building model and suggested that the distinctive detailing of vertical IMCs can influence the plastic hinge-formation mechanism and the distribution of inelasticity between upper and lower level columns. Gunawardena et al. [6] developed a purely modular structural system and assessed its behaviour under seismic loads through non-linear time history analyses against six earthquake ground motions using a 10-storey model in RUAUMOKO 3D®, concluding that the IMCs are essential contributors to the lateral force resisting system (LFRS) of steel MBSs. Srisangeerthanan et al. [7] used MATLAB® and OpenSees® to measure the diaphragm service stiffness of a 4-storey MBS under 44 scaled ground motions along the weak axis of the volumetric module floor diaphragm and observed that changing diaphragm flexibility by considering specific behaviours for IMCs affects the mode participation, inter-storey drifts and connection forces. Chua et al. [8] studied the influence of simplified modelling of IMCs by subjecting a 40-storey steel MBS to wind loads and concluded that horizontal IMCs played vital roles in resisting lateral forces. Lacey et al. [9] investigated a 6-storey steel MBS under wind and seismic actions using SAP2000® and highlighted that the overall response to lateral loads was highly dependent on the different stiffnesses of IMCs. In a recent optimality criteria-based minimum-weight optimisation study conducted on three-storey MBSs and a comparative moment resisting frame (MRF) benchmark structure, Wang and Tsavdaridis [10] revealed that while the flexural rigidity of vertical IMCs did not play a significant role in the overall lateral stiffness of unbraced MBSs, having hinged IMCs at each level equated to a diaphragm discontinuity which caused the optimised MBS to be heavier than the optimised benchmark MRF under the same target frequency constraint. Hence, from a system-level perspective there is a clear consensus among researchers that IMCs play a crucial role in the structural behaviour of high-rise steel MBSs during earthquake or wind loading.

The behaviour of IMCs from a component-level perspective has also attracted a great deal of attention, leading to numerous studies which developed new connections and investigated their force resisting mechanisms, failure modes, and nonlinear mechanical properties. So far, studies which carried out cyclic loading protocols to characterise the hysteretic behaviours of steel MBS joint assemblies revealed that most IMCs were designed to work in the elastic state, while ultimate failure occurred either in the column-endplate interface [11], beams [12–16] or in beam-column interfaces [17,18]. However, designing the global plastic-hinge formation mechanism to be heavily reliant on the hysteresis of the steel framing member leads to costly and impractical retrofitting programmes or even demolition, particularly in high-rise steel MBSs where more complex and demanding load transfer paths severely impact the damage levels in the volumetric modules.

1.2. Resilience of IMCs

To unlock the full “disassembly and reuse” potential of steel MBSs, it is necessary to put more effort into devising IMCs with improved ductility and energy dissipation, harnessed by specific components which are easy to repair, retrofit or replace and which can contribute effectively to the overall damage distribution mechanism of the structure, preventing the concentration of plastic stresses and strains in the framing members of volumetric modules. Although the potential benefits of developing smart IMCs, by means of passive damage control to improve the resilience of steel MBSs have been identified in the past [3,7,19,20], the volume of published studies around this topic is still limited. Sultana and Youssef [21] investigated the effect of superelastic shape-memory alloy (SMA) bolts in vertical IMCs of a 6-storey steel MBS using SeismoStruct® and revealed that adopting SMA IMCs in specific locations reduced residual drifts and improved damage distribution without significant increase of maximum inter-storey drifts. The study only considered the effect of SMA IMCs on the global behaviour of steel MBSs, without focusing on the implications of using SMA bolts on the working mechanisms, failure modes and local behaviour of IMCs. Wu et al. [22] studied the effects of a shock-absorbing IMC on the seismic behaviour of 2-storey container buildings using FEA software Abaqus® and found that the lead rubber bearing placed between volumetric modules delivered a fuller hysteretic curve, reduced stresses in frame elements, and decreased yield area and strength degradation post-yield. Nevertheless, the use of connection parts made of lead is detrimental to the overall sustainability of MBSs due to health and pollution risks during lead production. Jing et al. [23] developed a slider device with bonded rubber units (BRUs) integrated in the wall tracks of volumetric modules and discovered that due to the hyperelasticity of rubber the BRU could suffer large deformation without failing or losing its self-recovery ability. The system’s applicability is limited to MBSs made of cold-formed steel sections. Sendanayake et al. [11] conducted both experimental and numerical analyses on an IMC subjected to cyclic lateral loading and attributed the improved energy dissipation and the ability to shift the damage away from critical framing members to the addition of rubber pads between the endplates of columns. The configuration did not include means of re-centring, and the investigation was carried out on double stub-column specimens with relatively short lengths, which influenced the moment – rotation curves reported. The findings reported so far support the need for further research into the development of smart and resilient IMCs by means of employing passive damage control methods.

1.3. Properties of high-damping rubber (HDR) dissipative devices

In the past decades, the use of high-damping rubber (HDR) in dissipating devices for passive damage control of conventional MRFs has gained a lot of traction, in a pursuit to increase the low inherent damping representative of high-rise steel buildings [24]. HDR inherits the nearly-incompressible behaviour, large elastic strain capacity, recoverability and hysteresis of unfilled rubber [25], while also benefiting from improved damping due to the addition of carbon black filler [26]. These favourable characteristics can enhance hybrid natural rubber bearings (NRBs) with viscous or metallic dampers [27,28], supporting the development of HDR-based dissipative devices [26,29–31] and bearings [32–34]. However, while effective in dissipating energy, HDR bearings can introduce excessive displacement and permanent residual drifts during high intensity wind or seismic actions because of their limited shear stiffness.

1.4. Properties of hybrid HDR-SMA dissipative devices

Recently, a new trend of hybrid dissipative devices has emerged, combining the viscoelasticity of rubber with the strain recovery of smart alloys (shape-memory alloys or SMAs) such as Nickel-Titanium (also known as Ni-Ti or nitinol). SMAs are a class of smart materials with physical properties comparable to those of structural steel, capable of ‘memorising’ their shape due to the reversible transitions between its two main phases (i.e., martensite and austenite) caused by a shear lattice distortion mechanism [35]. The crystal structures of the two SMA phases are temperature-dependant: austenite is stable at high temperature, while martensite at low temperature [36]. For civil engineering applications, Ni-Ti can be manufactured in austenite phase at a wide range of desirable working temperatures, which enables austenitic Ni-Ti components to manifest the superelastic (or pseudoelastic) effect (SE), characterised by the ability to accommodate large strains (as high as 8–10%) under loading and recover their initial shape when unloaded [37]. Moreover, bespoke attributes such as the ability to dissipate energy through stable cyclic hysteresis, high damping, combined with excellent fatigue and corrosion resistance have fostered the application of Ni-Ti components in passive damage control devices [38,39]. The effectiveness of hybrid rubber-SMA passive damage control devices has been demonstrated on a wide range of applications [40–45], while the

promising results revealed by more recent research on hybrid HDR-SMA devices have been of particular interest for the purpose of the present study [46–48].

Consequently, the evidence presented so far indicates that a relatively new generation of hybrid passive damage control devices, namely high-damping rubber shape-memory alloy (HDR-SMA) dissipative devices can be effective in improving the ductility, energy dissipation, damping, and residual drifts of steel structures. In a recent review amassing sixty IMCs from the literature, the authors have identified the potential of enhancing resilience of high-rise steel MBSs by using rubber components and SMAs in IMCs and highlighted that such configurations have been explored up to a very limited extent [49]. Furthermore, there has been no account of adopting neither HDR nor hybrid HDR-SMA in the development of IMCs for steel MBSs, leaving room for further investigations to narrow this gap.

Therefore, to address these limitations and research gaps, the present study proposes a novel, hybrid IMC using custom corner fittings, a high-damping rubber core and a shape-memory alloy bolt. The smart and resilient IMC assists in the passive damage control of steel MBSs during lateral loading by reducing the inelastic deformation developed in the framing members and dispersing the effects throughout the building's structure (i.e., effectively enabling a decentralisation of the global damage distribution mechanism by taking advantage of the numerous IMC points typically present in steel MBSs.). The practical value of this novel connection is fostered by the successful employment of unique mechanical properties of SMAs and HDR to improve the retrofitting, rehabilitation, reclaim and reuse opportunities for next-generation, sustainable MBSs. To this end, the structural behaviour of the proposed IMC has been fully characterised using high-fidelity finite element (FE) models by studying its mechanical response in tension and combined compression and shear.

2. The proposed hybrid IMC

The system has been developed to connect corner-supported volumetric modules made with hot-rolled steel members joined by custom corner fittings. In the conceptual design phase, various preliminary connection configurations have been explored with the objective of improving damage control and demountability while satisfying structural, constructional, and manufacturing constraints. A heuristic FEA optimisation has informed the present design by studying the use of high-strength steel bolts, the effect of length, number and layout of bolts, the influence of slotted bolt holes and types of washers, and the presence of supplementary yielding components to enhance energy dissipation.

The proposed connection system comprises a resilient core represented by a high-damping rubber bearing (HDRB) installed between the corner fittings of volumetric modules and a pseudoelastic bolt made of Ni-Ti based SMA. The conceptual details of the hybrid IMC are illustrated in Fig. 1. For clarity, only the main framing members (i.e., beams, columns, corner fittings) of the modules are illustrated, yet it has been considered implicit that floor and roof cassettes, walls, lateral stability systems as well as MEP systems are also included in ready-to-install fully finished modules.

The main advantages of the developed IMC are threefold: (1) demountable design using bolted joints, (2) supplementary damping on account of the HDR core, and (3) improved energy dissipation and

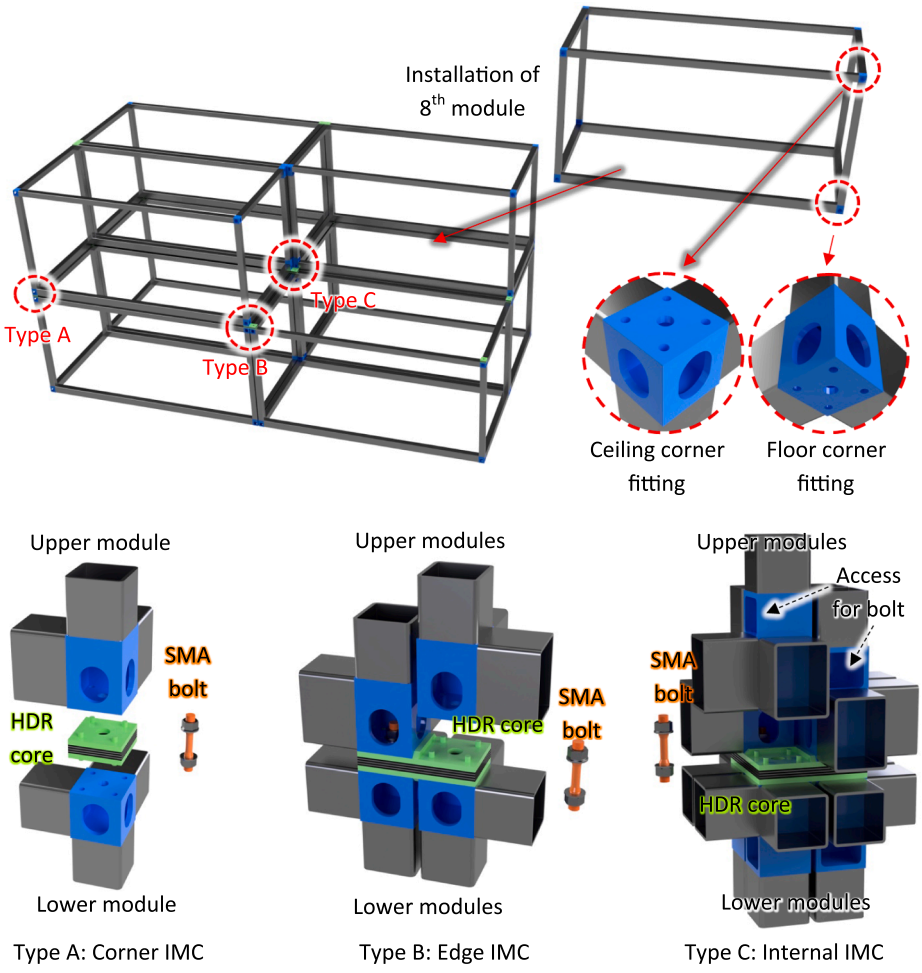

Fig. 1. Illustration of the proposed hybrid IMC.

reduced lateral drifts by virtue of the superelastic response of the SMA bolt.

To facilitate positioning of the volumetric modules, guiding lugs are provided on the outer plates of the HDRB with matching holes in corner fittings to accommodate the necessary level of constructional tolerances. The alignment of the double end threaded stud through the centreline of columns promotes a scalable and flexible design by keeping a simple and symmetric configuration with the same mechanical characteristics in both plan directions. This configuration ensures that load paths are provided explicitly through the rigid corners of the volumetric modules and placing the bolt inside the corner fittings provides an additional layer of protection from fire or thermal expansion. For corner and external joints (Type-C and Type-B), tensioning of the SMA bolts can be achieved through the access holes provided in corner fittings. While the challenge of securing the internal joint has been addressed before by either moving the connection in the beams [13,17] or using automatic devices [15,50], to avoid cutting holes in structural members and reduce their load bearing capacity, an alternative solution is considered herein. Corner fittings are extended to integrate access holes instead of weakening the module frame members.

As the hybrid IMC consists of bespoke steel, rubber and shape-memory alloy parts, the material consumption of the proposed solution needs some consideration. Of particular interest is the matter of increasing material usage in the case of connection duplication with each building level added. In this regard, it must be mentioned that in order to achieve an efficient use of material, the connection configuration needs to be optimised to meet specific performance design constraints at each floor level. The impact of connection repeatability due to building scale may be further lowered by determining whether the developed solution is needed only at specific levels along the building height to achieve a desirable global response. A global study (at macro-level) including parameters such as site location, building height, or lateral load type and magnitude is required to prove this.

2.1. The role of the resilient core

The HDR core has two main functions and is regarded both as a bearing and a dissipative device. Firstly, it provides evenly distributed and continuous vertical load paths between volumetric modules through the outer plates made of structural steel, while the (nearly) incompressible rubber layers reinforced with steel shims can withstand large compressive stresses. Secondly, it accommodates inter-storey shear forces and lateral drifts by undergoing large elastic strains without failing, alleviating the high-stress force-transfer zones at the corners of volumetric modules and, thus preventing the development of plastic damage in the structural framing. The lugs on the outer plates also play a structural role, acting as stoppers in the later stages of post bolt-failure, ensuring the stability of the structural frame until the commencement of retrofitting works. While recently, the use of laminated double beams has been promoted for the beneficial composite effect [51,52], the small gap introduced by the HDRB is deemed beneficial for the structural flexibility of volumetric modules, as designing floor and ceiling beams to take load independently allows future repurpose or relocation if architectural layout changes are desired during the life cycle of the MBS. Moreover, the gap created between ceiling and floor beams can be used to accommodate building services while the air barrier provides additional fire resistance and improves the acoustic performance of the modular structure [53].

2.2. The role of the pseudoelastic SMA bolt

The pseudoelastic SMA bolt serves two complementary structural functions: one is to provide uplift (tension) resistance to the joint through the clamping action generated by preload, while the other is to resist inter-storey drifts through a combined bending and shear action.

However, the main benefits of the proposed IMC are furnished by the pseudoelastic response of austenitic Ni-Ti based SMA which allows the shank to undergo large elastic strains (up to 5–6%) and recover its initial shape without failing. In the context of the present study, this effect equates to easy dismantling after damage-inducing events such as intense winds or earthquakes, as opposed to HS steel bolts which either fail or become jammed. In addition, considerable energy dissipation and damping are supplied through hysteresis during the cyclic transition between austenite–martensite phases of the smart alloy.

Among the limitations of the proposed IMC there can be a relatively high manufacturing cost for the SMA bolt, yet the cost may be offset by the gains related to the elimination of damage in the framing members improving reclaim and reuse prospects. Also, substantial advancements have been made in the technologies of manufacturing and processing smart alloys, specifically through the successful implementation of additive manufacturing techniques such as selective laser melting (SLM) or direct energy deposition (DED) [54,55] which mitigate the need for difficult machining processes, while further breakthroughs in this area are expected to drop future manufacturing costs for smart alloys.

3. Methodology

3.1. Study framework

In the present study, the hybrid response of the proposed IMC has been analysed by carrying out detailed continuum finite-element simulations using highly nonlinear material models calibrated with data from experimental material characterisation tests. A summary of the complete process is illustrated in Fig. 2.

Validated high-fidelity FEA has facilitated the proof-of-concept connection tests undertaken to determine the mechanical behaviour of the hybrid IMCs with respect to two translational degrees-of-freedom (DOFs) of interest namely, axial tension and combined compression and horizontal shear. The DOFs selected correspond to the main deformation modes expected to be sustained by the proposed IMCs in the structural system of high-rise steel MBSs under the combined effect of vertical and horizontal loading. The influence of relevant structural parameters has been determined for each loading mode. Constitutive models have been calibrated using experimental test data to realistically reflect the stress–strain response expected from the adopted materials. The FEA test results have been used to fully characterise the mechanical behaviour of the novel connection by determining the deformation modes, strength, stiffness, ductility, energy dissipation and damping capabilities for all relevant connection components as well as their individual contributions to the overall hybrid mechanical response. According to the different levels of experimental testing for inter-module joints identified by Lacey et al. [56], the adopted connection test configurations consist of the inter-module connection (IMC) zone without consideration of beam-column (BC) sub-assemblages, in order to capture the pure structural contribution of the IMC within a prospective inter-module joint (IMJ) and to facilitate the extraction of these structural behaviours for prospective development of simplified joint models.

3.2. High-fidelity finite element analysis (FEA)

The computational analyses in the present study have been conducted using the standard (implicit) solver of commercial FEA package Abaqus® [57]. The FEA model setup, test specimens and material model calibrations are discussed below.

A parametric study is conducted to determine the influence of important test parameters on the hybrid IMC's tension and combined compression-shear behaviours. For tension FEA, the selected parameters are bolt preload, $F_{p.C}$, and thickness of corner fitting's endplate, t_{cfe}, while for shear FEA, the studied parameters are magnitude of compressive axial load, N_{Ed}, and vertical layer (VL) layout of the HDR core. The bolt preload is determined based on a corresponding pre-stress level in the SMA bolts' shank, σ_{pre}. To provide initial stiffness without

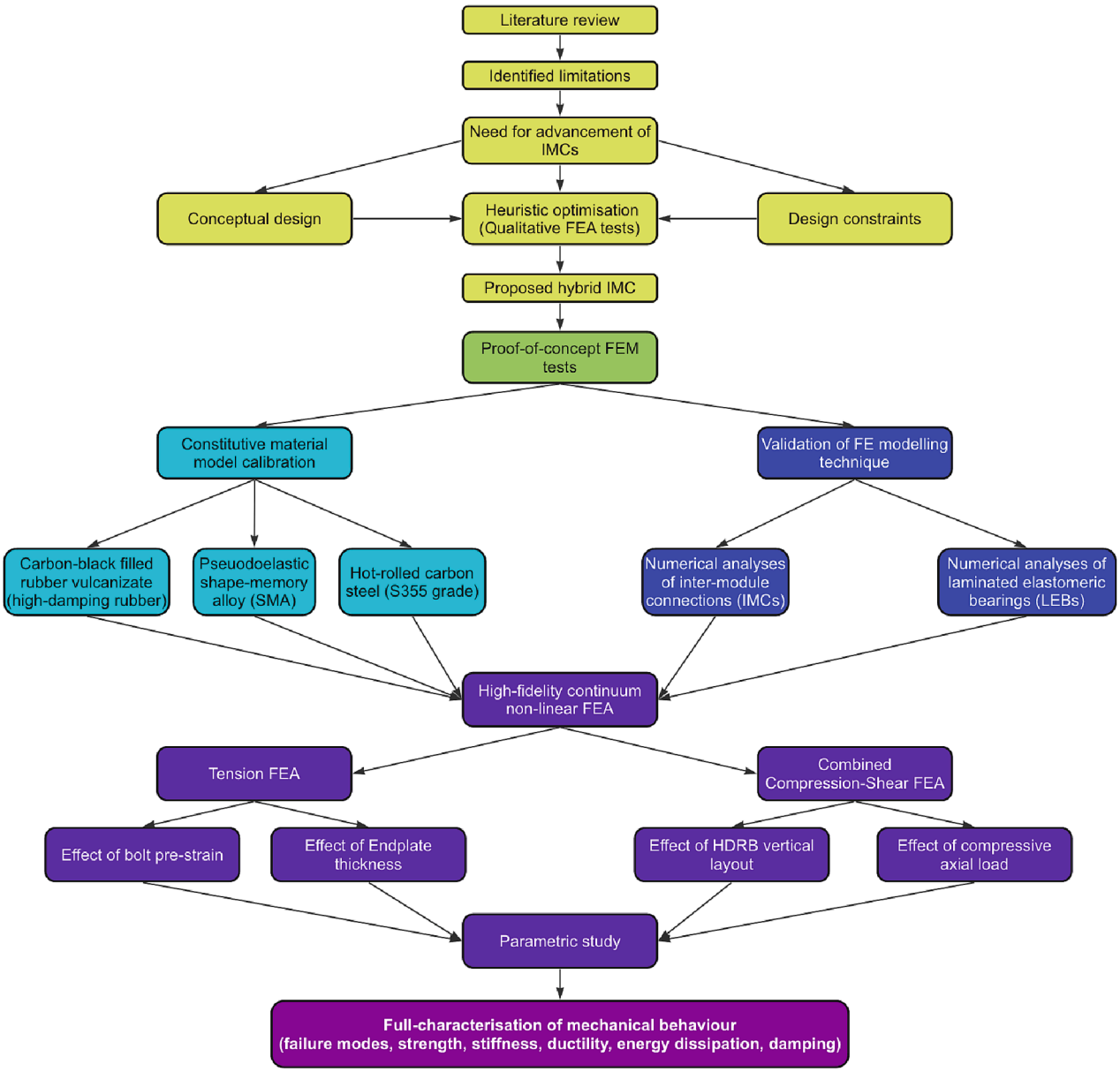

Fig. 2. Overview of the present study.

affecting the ductility and re-centring capability of the bolts, the pre-stress in the bolts is limited to 50% and 100% of the forward transformation start stress, σ_{Ms}. To simulate the effect of permanent gravitational loading on the shear behaviour of the hybrid IMC, axial load, N_{Ed}, equal to 5% and 10 % of the compressive yield capacity ($N_{c.Rd}$) of the column's cross-section is adopted, as per Lacey et al. [56]. The two axial load magnitudes applied to the hybrid IMC, combined in turn with one of the two bolt preloads are equivalent to compressive stresses on the HDR core ranging from 8.35 MPa (for **"N05-P50"** specimens) up to 16.9 MPa (for **"N10-P100"** specimens). While these values represent a rather upper bound limit from the perspective of maximum compressive stresses recommended by design codes [58,59], the decision is justified as the typical layout of building structures such as tall, self-standing MBSs results in higher axial load distribution per column, hence subjecting the HDR cores in such applications to higher compressive stresses. A summary of the test matrix and studied parameters is reported in Table 1.

$$N_{c.Rd} = (Af_y)/\gamma_{M0} \quad (1)$$

$$F_{p.C} = A_s\sigma_{pre} \quad (2)$$

3.3. FEA model setup

A highly nonlinear FEA setup is employed, including all three types of nonlinearities, namely geometric, material and boundary. All contact interactions are modelled using surface-to-surface discretisation with finite sliding formulation. The complete definition of contact between all joint components includes contact surfaces for the bolt, the HDRB, and the corner fittings. Normal behaviour is defined using the nonlinear, penalty-enforced, "Hard" pressure-overclosure relationship, while for tangential direction, the default penalty friction formulation based on the basic Coulomb friction model is adopted. A friction coefficient $\mu = 0.3$ has been adopted, assuming steel-to-steel interfaces that have been cleaned by wire-brushing or flame cleaning, with loose rust removed as per EN-1090–2 [61]. The unsymmetrical matrix storage and solution scheme is used to cater for the friction coefficient $\mu > 0.2$. The HDRB components (outer plates, steel shims and elastomer layers) are created separately, and an ideal, error-free adhesive steel-rubber bond is

Table 1
Test specimen matrix.

	Specimen ID	N_{Ed} (kN)	$F_{p.C}$ (kN)	t_{cfe} (mm)	VL layout
Tension FEA	P50-E15	–	$50\%\sigma_{Ms} = 80$	15	VL1
	P50-E20	–	$50\%\sigma_{Ms} = 80$	20	VL1
	P50-E25	–	$50\%\sigma_{Ms} = 80$	25	VL1
	P100-E15	–	$100\%\sigma_{Ms} = 160$	15	VL1
	P100-E20	–	$100\%\sigma_{Ms} = 160$	20	VL1
	P100-E25	–	$100\%\sigma_{Ms} = 160$	25	VL1
Shear FEA	N05-P50-VL1	$5\%N_{c.Rd} = 97.5$	$50\%\sigma_{Ms} = 80$	15	VL1
	N05-P50-VL2	$5\%N_{c.Rd} = 97.5$	$50\%\sigma_{Ms} = 80$	15	VL2
	N05-P100-VL1	$5\%N_{c.Rd} = 97.5$	$100\%\sigma_{Ms} = 160$	15	VL1
	N05-P100-VL2	$5\%N_{c.Rd} = 97.5$	$100\%\sigma_{Ms} = 160$	15	VL2
	N10-P50-VL1	$10\%N_{c.Rd} = 195$	$50\%\sigma_{Ms} = 80$	15	VL1
	N10-P50-VL2	$10\%N_{c.Rd} = 195$	$50\%\sigma_{Ms} = 80$	15	VL2
	N10-P100-VL1	$10\%N_{c.Rd} = 195$	$100\%\sigma_{Ms} = 160$	15	VL1
	N10-P100-VL2	$10\%N_{c.Rd} = 195$	$100\%\sigma_{Ms} = 160$	15	VL2

Notes: $N_{c.Rd}$ is the design resistance of the cross-section for uniform compression as defined in Eurocode 3 [60] and is calculated using expression (1), for members not susceptible to local buckling failure, where A is the cross-sectional area, f_y is the yield strength of steel, and γ_{M0} is a partial safety factor. Results are based on a hot-rolled Celsius® SHS150x10 column cross-section of S355 steel grade. Bolt preload, $F_{p.C}$, is given by expression (2), where A_s is the cross-sectional area of the bolt shank and σ_{pre} is the pre-stress level in the bolt shank.

assumed by merging all components into a single part while preserving geometric boundaries and material properties. This method is preferred to reduce the computational demand on the analysis required by defining numerous contact constraints.

General static steps are defined for each loading stage. The initial bolt preload is applied during the first step in both tension and shear FEA. For the tension FEA setup, a displacement-controlled vertical load is applied during the second step, while for the shear FEA a compressive axial load is applied in the second step, followed by a displacement-controlled horizontal shear loading during the third step. Loading and boundary conditions are applied using reference points coupled to cross-sections with distributed continuum coupling constraints, while the bolt pre-tension is defined through an orthogonal surface passing through the middle of the bolt's shank. The cyclic loading histories for tension and shear FEA are illustrated in Fig. 3. The EN 15129 loading protocol [59] is used in the tension FEA, with three positive-only cycles at $+0.25\ \Delta_{bd}$, $+0.5\ \Delta_{bd}$, $+\Delta_{bd}$, where Δ_{bd} is the design displacement limited to the maximum displacement, Δ_{max}, corresponding to the displacement at which the stress in the bolt's shank reaches the finish transformation stress σ_{Mf}. The maximum displacement, Δ_{max}, has been determined through an initial monotonic tension loading sequence for each tested specimen. Same protocol is adopted for cyclic shear loading, this time with three fully reversed cycles of $\pm0.25\ \Delta_{bd}$, $\pm0.5\ \Delta_{bd}$, $\pm\Delta_{bd}$, where Δ_{bd} has been determined based on the same method as explained above.

All parts are rigorously partitioned to enable the use of structured mesh controls with Hex elements for better convergence. The steel and SMA parts have been meshed with first-order 8-node linear brick (3D solid) elements (C3D8R) with reduced integration, while the steel plates in the HDR core have been meshed with the equivalent hybrid elements (C3D8RH). The rubber layers have been meshed with fully integrated first-order 8-node hybrid linear brick elements (C3D8H). The adequate mesh refinement has been explored in terms of accuracy of results versus analysis efficiency. Following a rigorous sensitivity analysis, the connection parts have been discretised as follows. A minimum of three mesh elements are provided through the thickness of all thin-walled sections. The corner fittings are meshed with 5 mm global size elements, while the bolts are meshed with 2 mm global size elements. The HDR core is meshed with 4 mm global size elements, while the elastomer layers have 5 elements through the thickness of each layer. An overview of the FEA model setup and mesh details are illustrated in Fig. 4.

3.4. Test specimens

Design details of the connected corner fittings and adjoining post and beam segments are based on typical sizes of modular framing members reported in the literature [1]. The plan dimensions of the corner fittings top and bottom cover plates are 150 mm × 150 mm, to accommodate SHS150x10 hot-rolled square hollow steel corner posts. Vertical plates have constant thicknesses of 15 mm, while different depths have been chosen, depending on the depths of the adjoining floor and ceiling beam members. Rounded access holes of 100 mm × 80 mm and rounded corner radii of 40 mm are considered on two adjacent vertical plates in

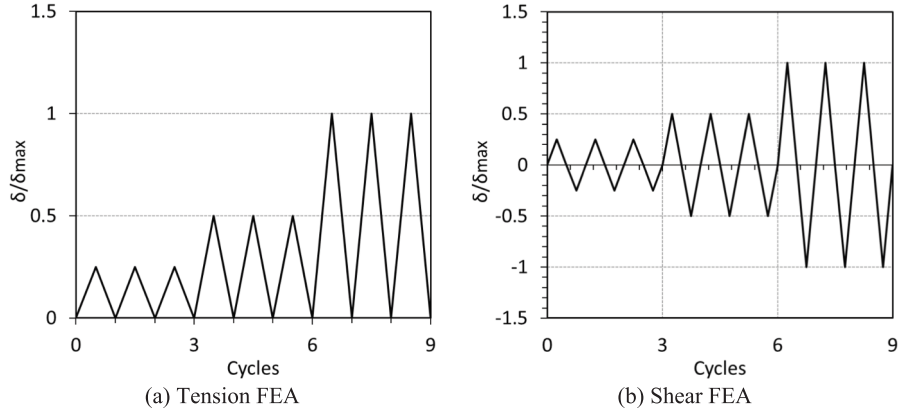

Fig. 3. Cyclic loading histories.

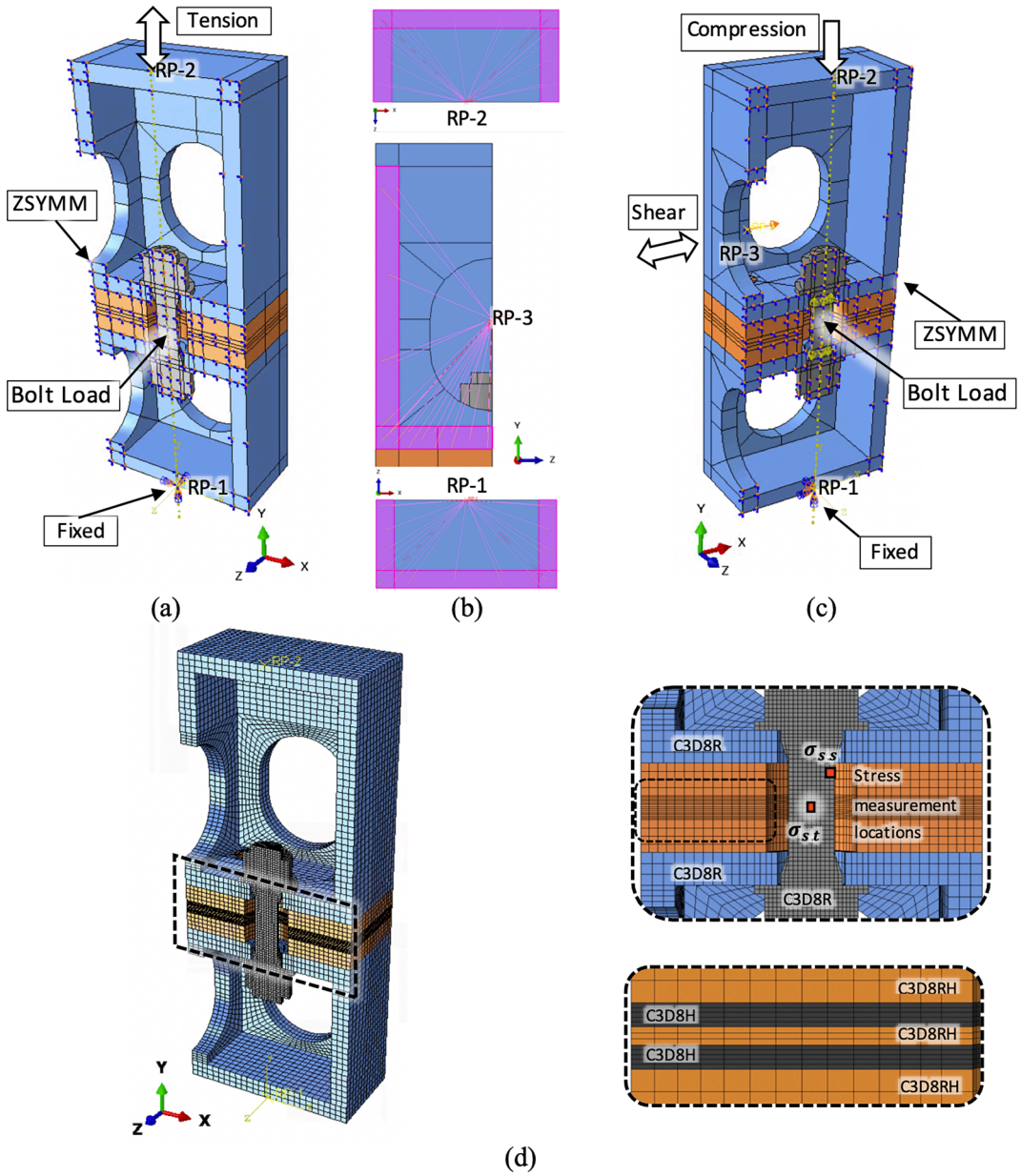

Fig. 4. Model setups: (a) tension FEA, (b) reference points coupling, (c) combined compression-shear FEA, (d) meshing details.

each corner fitting. Detailed drawings of the corner fittings are illustrated in Fig. 5 (a) and (b).

The preliminary design of the HDR cores is based on recommendations for elastomeric bearings as per EN 1337–3 [58]. All HDR cores considered herein have 150 mm × 150 mm square plan shapes to ensure flush alignment with the external surfaces of the vertical steel walls of corner fittings, while 3-mm-thick reinforcing steel shims and 15-mm-thick steel cover plates have been used throughout all bearing configurations adopted in this study. A large 40 mm diameter hole is placed at the centre of the HDR cores to ensure that the SMA pin does not come into contact with the inner sides of the HDR core at any time during cyclic shear loading. Given the constraint on the plan dimensions, a preliminary thickness of the elastomeric layers has been set to 4 mm to ensure a reasonable compressive stiffness of the HDRBs, described by a shape factor $S \cong 8.85$. The shape factor, S, is a property of the elastomeric bearing that relates the geometry of the bearing to its compressive stiffness and is given by expression (3) as per EN 1337–3 [62]. A summary of the sizes and layouts considered is reported in Fig. 5 (c).

$$S = \frac{A_1}{I_p t_e} \tag{3}$$

Where:

A_1- effective plan area of the bearing

I_p- force-free perimeter of the bearing

t_e- effective thickness of an individual elastomer layer in compression

A preliminary M20 net shank diameter has been adopted for the bolts, as the single-bolt configuration of the proposed IMC requires a reasonably large bolt diameter. When sizing the dog-bone shaped SMA bolts, special concern has been given to the threaded regions which are known as potentially vulnerable zones prone to premature fracture. Consequently, to ensure an adequate ductility, the SMA bolt samples have been dimensioned with net diameters of the threaded regions larger than the diameters of the shank regions, having net threaded-to-shank diameter ratio, $D_{th.net}/D_{sh.net}$, in the range of 1.2–1.3. This value is expected to ensure a fracture-free tensile strain of at least 6%, as suggested by Fang and Wang [35] based on experimental test observations reported in the literature [63–65]. Details of the diameters and ratio are

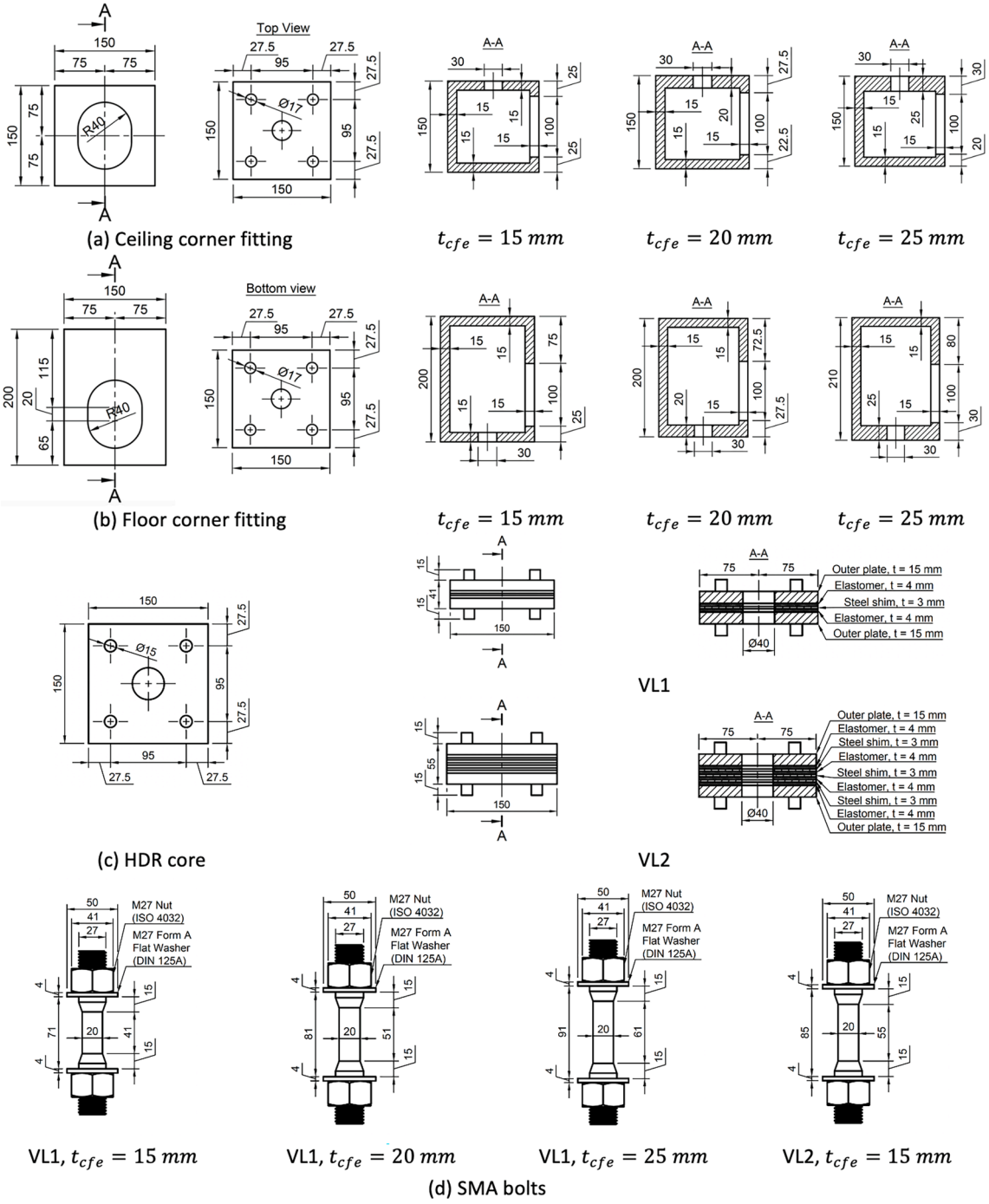

Fig. 5. Detailed drawings of specimen components (units in mm).

Table 2
Design considerations of the dog-bone shaped SMA bolt samples.

SMA bolt sample	D_{th} (mm)	$D_{th.net}$ (mm)	$D_{sh.net}$ (mm)	$D_{th.net}/D_{sh.net}$
M20-27	27	25	20	1.25

reported in Table 2, while detailed drawings are illustrated in Fig. 5 (d).

3.5. Experimental tests for material model calibration

To calibrate the advanced material models required for capturing the viscoplastic behaviour of high-damping rubber (HDR) and the pseudoelastic (superelastic) behaviour of austenitic shape-memory alloy (SMA), both materials were characterised through specific experimental testing. Details of test configurations, loading modes and protocols were laid out in the following paragraphs.

The ultra-high damping rubber compound from Tun Abdul Razak Research Centre (TARRC - https://tarrc.co.uk/) is adopted for the elastomeric layers of the HDR connector. Double-bonded shear tests have been carried out at TARRC on cylindrical test pieces made of two rubber layers hot-bonded to metal plates (Fig. 6 (a)). One test piece has been subjected to sinusoidal waveforms of 0.5 Hz frequency for 6 cycles at ± 1, ±2, ±5, ±10, ±20, ±50, ±100, ±150, ±200 % shear strains to determine the secant shear modulus, G, and the equivalent viscous damping ratio, ξ_{eq}, of HDR (Fig. 6 (b)), reported for the sixth cycle for

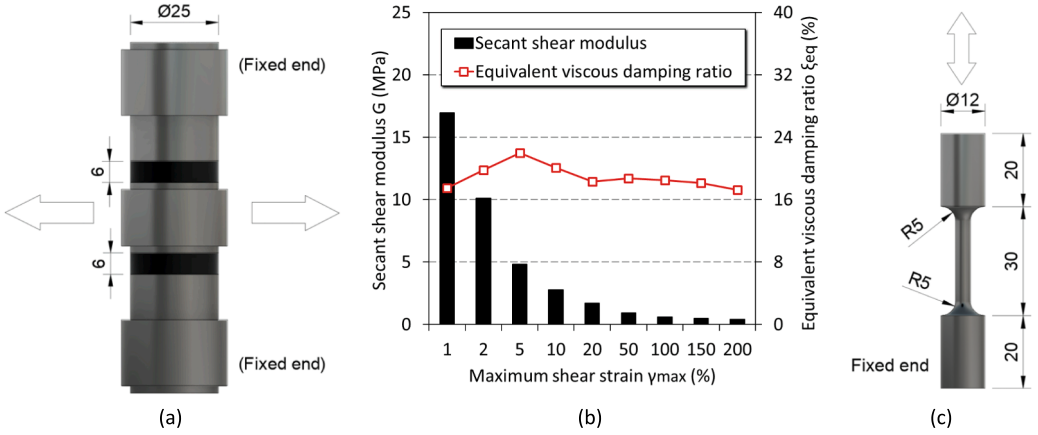

Fig. 6. Experimental test schemes for material model calibration: (a) rubber test pieces, (b) secant shear modulus of HDR, (c) SMA coupon.

each strain amplitude. The method for determining the respective parameters is described in more detail by Orfeo et al [66]. The experimental tests for FEA material model calibration have been done at ambient temperature and the test pieces have been subjected to triangular waveforms up to ±200% shear strain for 6 cycles at 10% strain rate (0.1/s) with a 2-minute wait before being subjected to triangular waveforms up to ±200% shear strain for 1 cycle over an amplitude range of 25% shear strain with stress relaxation segments of 2 min inserted between each step change. The 6 consecutive cycles of ±200% shear strain have been done to account for the cumulative damage (also known as Mullins damage), such that the calibration was done on an already stabilised stress–strain behaviour of the HDR. The load-relax-load incremental steps are necessary for the calibration of the hysteresis parameters of the Bergström-Boyce model, which requires test data for at least two different strain rates to accurately predict the desired mechanical behaviour.

The Ni-Ti based SMA adopted is a Ni-rich Ni-Ti alloy (51Ni-49Ti % at.) supplied by the company 2SMArtEST Srl (https://2smartest.com/). The dog-bone samples have been heat treated at about 500 °C for 30 min to adjust the final transformation temperatures (austenite finish temperature $A_f \approx 0$ °C) and give proper superelastic behavior at a practical range of temperatures for real-life applications.

Isothermal mechanical tests for material characterisation consisting of pseudo-static cyclic tensile tests with a monotonic strain controlled loading ($\dot{\varepsilon} = 3{\cdot}10^{-4}$ s^{-1}) up to a given strain, ε_{tot}, followed by complete load-controlled unloading ($\dot{\sigma} = 12$ MPa·s^{-1}) have been performed at University of Calabria on standard dog-bone test pieces (Fig. 6 (c)) in fully austenitic conditions (T = 20 °C). The tests have been carried out by using a universal testing machine (Instron E10000, USA) and strains have been measured by an extensometer (accuracy class 0.5 ISO) with a gauge length of 10 mm.

Data in the form of stress–strain and load–displacement curves has been extracted from the experimental tests detailed above and has been used for calibration and validation of the material models, as described in the following sections.

3.6. Constitutive material models

The theoretical formulations and calibration studies behind the advanced non-linear material models employed to define the mechanical behaviour of hot-rolled carbon steel, high-damping rubber, and austenitic SMA have been presented in the following paragraphs.

3.6.1. Hot-rolled carbon steel

In Abaqus®, the material library offers a variety of mechanical constitutive models to describe the behaviour of metals for implementation in stress analysis problems. Based on the assumption of an additive relationship between strain rates (expression (4)) to decompose the deformation into elastic (recoverable) and inelastic (non-recoverable) parts, the full mechanical response of structural steel has been defined through a combination of complementary material behaviours such as elasticity and plasticity.

$$\dot{\boldsymbol{\varepsilon}} = \dot{\boldsymbol{\varepsilon}}^{el} + \dot{\boldsymbol{\varepsilon}}^{pl} \tag{4}$$

Where:

$\dot{\boldsymbol{\varepsilon}}$- the total strain rate

$\dot{\boldsymbol{\varepsilon}}^{el}$- the rate of change of the elastic strain

$\dot{\boldsymbol{\varepsilon}}^{pl}$- the rate of change of inelastic strain

An appropriate elastic response model for steel is the isotropic linear elasticity represented by expression (5), indicating that stress is proportional to the applied strain and independent of the direction at a material point. This is a legitimate approximation because the elastic strains are small, of order 10^{-3} (the yield stress being three orders of magnitude smaller than the elastic modulus) [67].

$$\boldsymbol{\sigma} = \boldsymbol{D}^{el}\boldsymbol{\varepsilon}^{el} \tag{5}$$

Where:

$\boldsymbol{\sigma}$- the total stress state of a material point

$\boldsymbol{D}^{el}$- the fourth order elasticity tensor that is independent on the deformation

$\boldsymbol{\varepsilon}^{el}$- the total elastic strain state of a material point

For the inelastic response of steel, a classical metal plasticity, rate-independent model using the Mises yield surface with associated plastic flow and isotropic hardening has been chosen. When defining plasticity in Abaqus®, a final step before the input of material data is the conversion of nominal (engineering) stress and strain values (σ_{nom}, ε_{nom}) to true stress and logarithmic plastic strain (σ_{true}, ε_{ln}^{pl}) for the solver to properly interpret the data. This is since the inelastic response of hot-rolled carbon steel occurs over a strain range which no longer belongs to the domain of small-strain theory (up to 16% ultimate tensile strain) which is formulated in terms of total stress and total strain values. Hence, it is necessary to adopt the finite-strain formulation which is defined in terms of "true" or Cauchy stress and logarithmic strain [67]. The conversion can be easily done using expressions (6)-(8).

$$\sigma_{true} = \sigma_{nom}(1 + \varepsilon_{nom}) \tag{6}$$

$$\varepsilon_{ln} = \ln(1 + \varepsilon_{nom}) \tag{7}$$

$$\varepsilon_{ln}^{pl} = \varepsilon_{ln}^{tot} - \frac{\sigma_{true}}{E} \tag{8}$$

Where:

σ_{true}– true stress (MPa)

σ_{nom}– nominal stress (MPa)
ε_{nom}– nominal strain (%)
ε_{ln}^{tot}– logarithmic total strain (%)
ε_{ln}^{pl}– logarithmic plastic strain (%)

To describe the inelastic behaviour of hot-rolled carbon steel, the standardised bi-linear plus nonlinear hardening model defined by expressions (9)-(11) proposed by Yun and Gardner [68] has been adopted in this study due to its practicality, being able to accurately represent the stress–strain response of steel based just on the three basic material parameters readily available in design codes, namely the modulus of elasticity E, the yield strength f_y, and the ultimate strength f_u. The model is more accurate than other typical models available in the literature (i.e., the elastic, perfectly plastic [60], the elastic, linear hardening, the tri-linear [69] or the Ramberg-Osgood model [70]) as it captures the elastic, yield plateau, and rounded strain hardening with progressive loss of stiffness regimes.

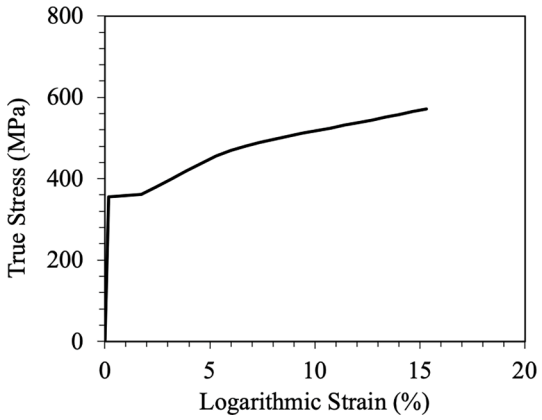

Fig. 7. Constitutive material models for structural steel.

$$f(\varepsilon)=\begin{cases} E\varepsilon, \varepsilon < \varepsilon_y \\ f_y, \varepsilon_y < \varepsilon \le \varepsilon_{sh} \\ f_y + (f_u - f_y)\left\{0.4\left(\frac{\varepsilon-\varepsilon_{sh}}{\varepsilon_u-\varepsilon_{sh}}\right) + 2\left(\frac{\varepsilon-\varepsilon_{sh}}{\varepsilon_u-\varepsilon_{sh}}\right) \Big/ \left[1+400\left(\frac{\varepsilon-\varepsilon_{sh}}{\varepsilon_u-\varepsilon_{sh}}\right)^5\right]^{1/5}\right\}, \varepsilon_{sh} < \varepsilon \le \varepsilon_u \end{cases} \quad (9)$$

$$\varepsilon_u = 0.6\left(1-\frac{f_y}{f_u}\right), \text{ but } \varepsilon_u \ge 0.06 \text{ for hot} - \text{rolled steels} \quad (10)$$

$$\varepsilon_{sh} = 0.1\frac{f_y}{f_u} - 0.055, \text{ but } 0.015 < \varepsilon_{sh} \le 0.03 \quad (11)$$

Where:
ε_u– true stress (MPa)
ε_{sh}– strain hardening strain

Material parameters used to characterise the elasto-plastic behaviour of steel grade S355 (Table 3) have been taken from Eurocode 3 [60] based on nominal material properties and nominal element thickness $t \le$ 40 mm. The corresponding (true) stress–strain curve is illustrated in Fig. 7.

3.6.2. *High-damping rubber*

Since linear elasticity is no longer fit for purpose to describe the highly non-linear time-dependent, large-strain mechanical behaviour of carbon-black filled rubber vulcanizates such as high-damping rubber, a different class of constitutive models called hyperelasticity is introduced, representing a non-linear generalisation of isotropic linear elasticity into the finite-strain domain.

Hyperelasticity in approximately incompressible isotropic elastomers can be described in terms of a strain-energy density function/potential (U), which relates the strain energy stored in the material per unit of reference volume to the strain in the material. While Abaqus® supplies a generous suite of strain-energy potentials, it is important to note that in cases where experimental test data is available for a single mode of deformation (such as the present study), it is advised to use particular forms based only on the first deviatoric strain invariant $\bar{I}_1$ (e.g., Neo-Hookean, Arruda-Boyce/Eight-Chain, Yeoh or Marlow/Response Function), as the influence of the second deviatoric strain invariant $\bar{I}_2$ is generally difficult to quantify and requires data from at least 2 different loading modes. Nevertheless, this simplification does not represent a significant sacrifice on precision, as it is widely accepted that in the case of filled elastomers, the $\bar{I}_2$-term in the strain-energy function is numerically close to 0 [71].

Of the $\bar{I}_1$-based models, the Yeoh form has been selected in this study for its ability to give the most accurate prediction of HDR's typical S-shaped stress–strain behaviour over the desired strain range, as demonstrated in the calibration studies (Fig. 8 (b)). Based on an additive decomposition of the deviatoric ($\bar{I}_1$) and volumetric (J_{el}) strain energy contributions, the Yeoh form of the strain-energy function [72] is given in Abaqus® as the third-order reduced polynomial illustrated in expressions (14)-(16) [67].

$$U = \sum_{i=1}^{3} C_{i0}(\bar{I}_1 - 3)^i + \sum_{i=1}^{3}\frac{1}{D_i}(J_{el}-1)^{2i} \quad (14)$$

$$\bar{I}_1 = \bar{\lambda}_1^2 + \bar{\lambda}_2^2 + \bar{\lambda}_3^2 \quad (15)$$

$$\bar{\lambda}_i = J^{-1/3}\lambda_i \quad (16)$$

Where:
U- strain-energy per unit of reference volume
C_{10}- coefficient representing the initial shear modulus at low strains
C_{20}- coefficient representing the softening effect at moderate strains
C_{30}- coefficient representing the "upturn" at higher strain levels
$\bar{I}_1$- first deviatoric strain invariant
D_i- temperature-dependent coefficients determining material compressibility

Table 3
Nominal material properties for steel grade S355.

Steel grade	ρ (kg/m^3)	E (N/mm^2)	ν (-)	f_y (N/mm^2)	f_u (N/mm^2)	ε_u (%)
S355	7,850	210,000	0.3	355	490	16.53

Note: (1) ρ is density of steel, (2) E is the modulus of elasticity, (3) ν is Poisson's ratio, (4) f_y is the yield strength, (5) f_u is the ultimate strength, (6) ε_u is the ultimate strain.

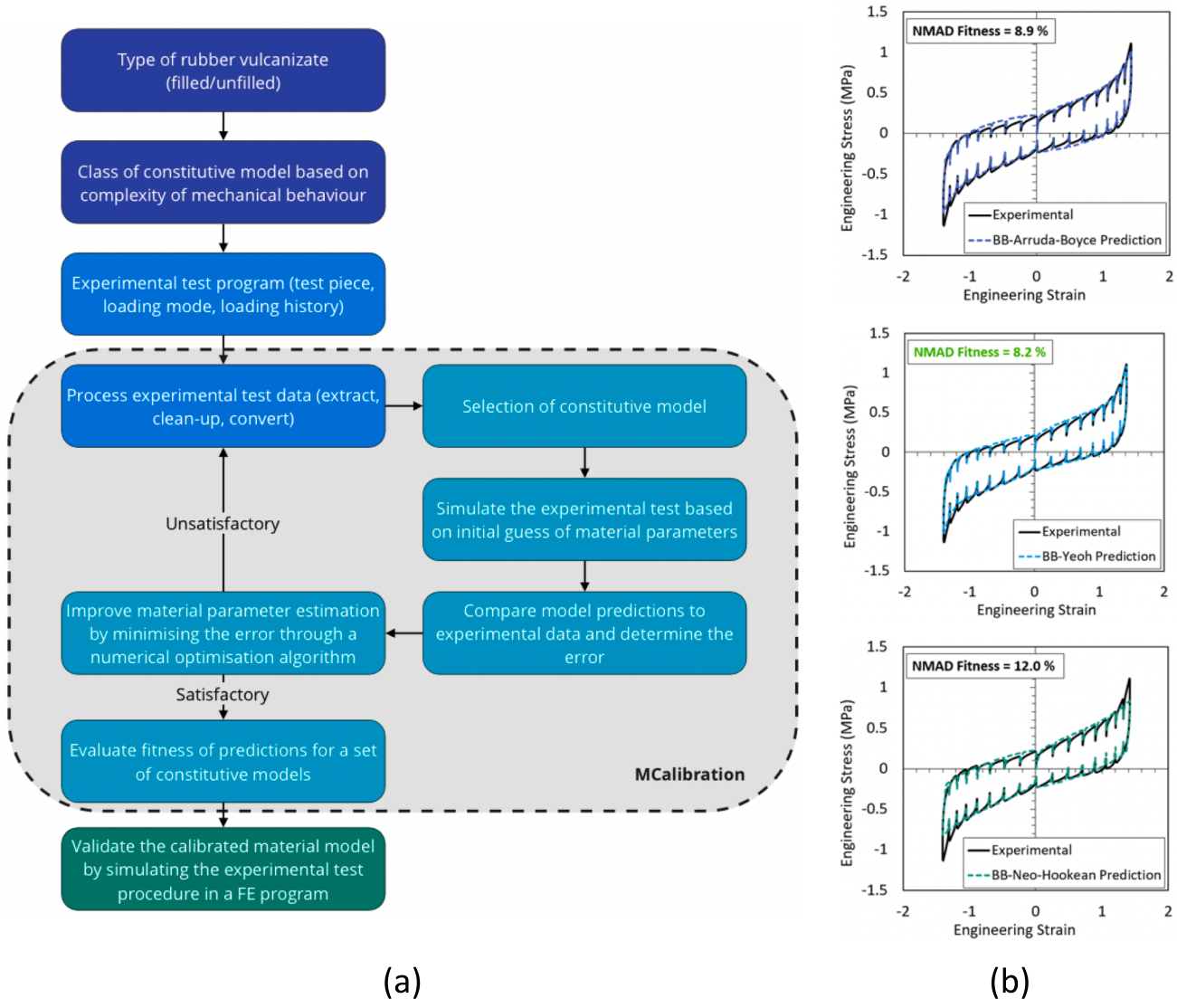

Fig. 8. Material calibration of HDR: (a) flow chart with full process, (b) calibrated models.

J_{el}- elastic volume strain
$\overline{\lambda}_i$- deviatoric stretches
λ_i- principal stretches
J- total volume strain

A hyperelastic model alone cannot be used to study the energy dissipation and damping properties of a HDR during cyclic loading because this class of models deals only with the elastic (instantaneous) behaviour ignoring the viscous (time-dependent) response, hence failing to capture the hysteresis. It is also unfit for capturing additional non-linearities such as the pronounced softening during initial load cycles due to damage accumulation in the material followed by stabilisation (known as Mullins damage) and progressive loss of stiffness with increasing strain amplitude (known as Payne effect). For this reason, the hyperelastic formulation needs to be expanded by means of linear viscoelastic (LVE) models or the more advanced, non-linear viscoelastic (non-LVE or viscoplastic) models. While linear viscoelasticity is generally useful in modelling elastomer-like materials, it is most accurate for the small-strain viscoelastic response of unfilled rubber compounds (i.e., low damping rubber) [66] and is therefore less adequate for the present study.

A powerful generalisation of linear viscoelasticity is the non-LVE constitutive model developed by Bergström and Boyce [25,73]. The model's theoretical formulation is rooted on the premise of decomposing the total stress response into an equilibrium response and a deviation from equilibrium response, and is represented by two parallel networks A (non-linear hyperelastic) and B (non-linear hyperelastic component in series with a non-linear viscoelastic flow element) [74]. In Abaqus®, the BB model can be employed as the 'Hysteresis' sub-option of 'Hyperelasticity', requiring the definition of four additional material parameters, namely a stress scaling factor (SF), creep parameter (A), effective stress exponent (m), and creep strain exponent (C).

Therefore, to properly capture the **non-linear viscoelastic** (non-LVE) response of TARRC's high-damping rubber, the constitutive material model adopted in Abaqus® has been defined using the **Bergström-Boyce (BB) model**, based on **Yeoh hyperelasticity**. The calibration of the material model has been performed using the commercial material parameter extraction tool MCalibration [75], which determines the material parameters for a given constitutive model and set of experimental data by treating the procedure as the non-linear mathematical minimization problem [74] defined by expression (17) as:

$$\min_{\boldsymbol{\xi}} \sum_{i=1}^{N} f(\boldsymbol{M}^i(\boldsymbol{\xi}) - \boldsymbol{E}^i) \tag{17}$$

Where:
$\boldsymbol{\xi}$- vector of material parameters to optimize

Table 4
Material properties for high-damping rubber.

Constitutive model	Hyperelasticity coefficients						Non-linear viscoelasticity (Bergström-Boyce)				NMAD Fitness
							SF	*A*	*m*	*C*	
Neo-Hookean	C_{10} 0.135	-	-	D_1 0	-	-	11.9	109.1	10.6	−1	12.0 %
Yeoh	C_{10} 0.139	C_{20} -0.014	C_{30} 0.003	D_1 0	D_2 0	D_3 0	24.7	141.4	10.85	−0.99	8.2 %
Arruda-Boyce	μ 0.166	λ_m 1.789	–	D 0	–	–	27.9	90.4	10.44	−0.96	8.9 %

Note: (1) C_{i0} are stiffness coefficients, (2) D_i are compressibility coefficients, (3) μ is the initial shear modulus coefficient, (4) λ_m is the locking stretch, (5) SF is the stress scaling factor, (6) A is the creep parameter, (7) m is the effective stress exponent, (8) C is the creep strain exponent, (9) NMAD is the Normalized Mean Absolute Difference/Error.

N- number of experimental data sets
$f(\bullet)$- coefficient representing the softening effect at moderate strains
$\boldsymbol{M}^i(\boldsymbol{\xi})$- model prediction of experimental data set i
$\boldsymbol{E}^i$- experimental data set i

This has been done to optimise the workflow, yet the same steps can also be performed through more time-consuming trial and error studies or by developing custom-made optimization routines using a general-purpose programming language of choice, both falling outside the scope of the present study. A flowchart outlining the complete process of calibrating and validating a constitutive model for rubber vulcanizates is illustrated in Fig. 8 (a). The material parameters corresponding to all non-LVE material models considered in the calibration studies were summarised in Table 4. All D_i terms defining material compressibility are taken as 0 to approximate the fully incompressible behaviour of elastomers.

3.6.3. Pseudoelastic shape-memory alloy

In order to accurately describe unique features of the mechanical behaviour of SMAs (e.g., the recovery of large deformations during load-unload cycles) that could not be represented by conventional inelastic models, an extension of the classical plasticity framework called generalised plasticity has been formulated [76]. On this basis, Auricchio and Taylor [77,78] have developed a constitutive model to characterise the pseudoelastic (superelastic) effect of SMAs at finite strains based on the typical uniaxial stress–strain response of phase transforming materials that illustrates a closed hysteresis (flag-shaped) loop as seen in Fig. 9.

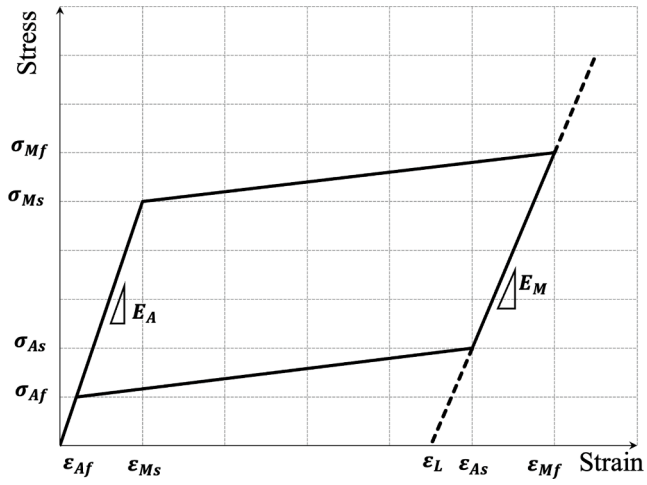

Fig. 9. Constitutive model of pseudoelastic Ni-Ti based SMA.

This constitutive model has a built-in formulation in Abaqus®/CAE and can be defined by using the Mechanical, Super Elasticity material behaviour when creating a new material. It is intended for modelling Ni-Ti based SMAs that undergo solid–solid, martensitic phase transformation and exhibit superelastic response [67]. Due to its practicality, it has been widely adopted in the literature and has accurately reflected the mechanical behaviour of Ni-Ti based SMA bars [79–85]. The following input material parameters need to be defined: Young's modulus and Poisson's ratio of austenite (E_A, ν_A), Young's modulus and Poisson's ratio of martensite (E_M, ν_M), the forward (load) transformation start stress σ_{Ms}, the forward (load) transformation finish stress σ_{Mf}, the reverse (unload) transformation start stress σ_{As}, the reverse (unload) transformation finish stress σ_{Af}, and the transformation strain ε_L. In the present study, the input data reported in Table 5 has been chosen from the inspection of the experimental stress–strain curve corresponding to the first load-unload cycle.

One limitation of this model is the inability to capture the degradation of the mechanical behaviour of pseudoelastic Ni-Ti based SMA. While alternative 'hybrid' modelling methods have been employed in the past with some success by introducing 'fake' steel fibres/layers characterised by metal plasticity with isotropic hardening [63,86–88], this technique is most appropriate for modelling SMA cables or strands rather than bolts, remaining impractical for general adoption.

3.7. FEA validation

The FEA conducted in this study is validated by simulating the experimental tests for three IMCs and a laminated elastomeric bearing. In addition, the validation of the calibrated material models presented in the previous section is also completed by simulating the experimental characterisation tests.

FEA validation I is conducted on the IMC with a rotary locking device studied by Chen et al. [89,90]. The experimental setups and corresponding numerical models are illustrated in Fig. 10. The validation results demonstrate the accuracy of present FEA in capturing the deformation modes and overall working mechanisms reported in the reference study. FEA validation II has been carried out on the post-tensioned IMC studied by Lacey et al. [91]. The experimental setup and corresponding numerical model can be seen in Fig. 11. The

Table 5
Material properties for constitutive model of pseudoelastic SMA.

E_A (MPa)	E_M (MPa)	ν_A	ν_M	σ_{Ms} (MPa)	σ_{Mf} (MPa)	σ_{As} (MPa)	σ_{Af} (MPa)	ε_L (%)
87,500	38,438	0.33	0.33	525	615	180	90	3.64

Note: (1) E_A is the Young's modulus of austenite, (2) E_M is the Young's modulus of martensite, (3) ν_A is the Poisson's ratio of austenite, (4) ν_M is the Poisson's ratio of martensite, (5) σ_{Ms} is the forward transformation start stress, (6) σ_{Mf} is the forward transformation finish stress, (7) σ_{As} is the reverse transformation start stress, (8) σ_{Af} is the reverse transformation finish stress, (9) ε_L is the total transformation strain.

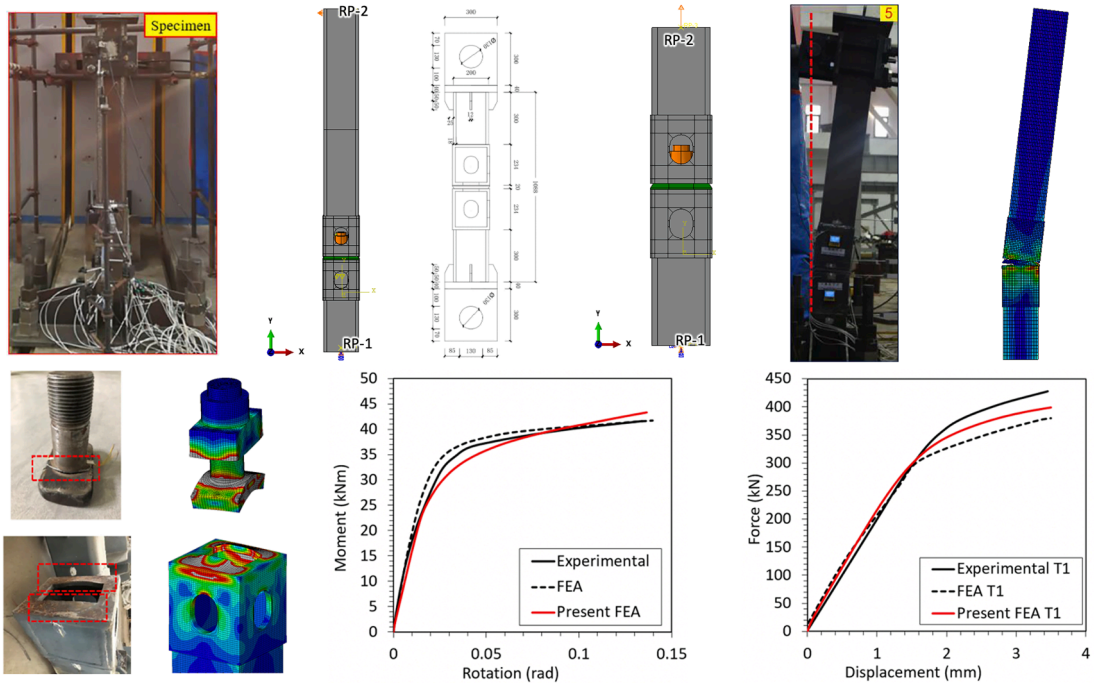

Fig. 10. FEA validation I.

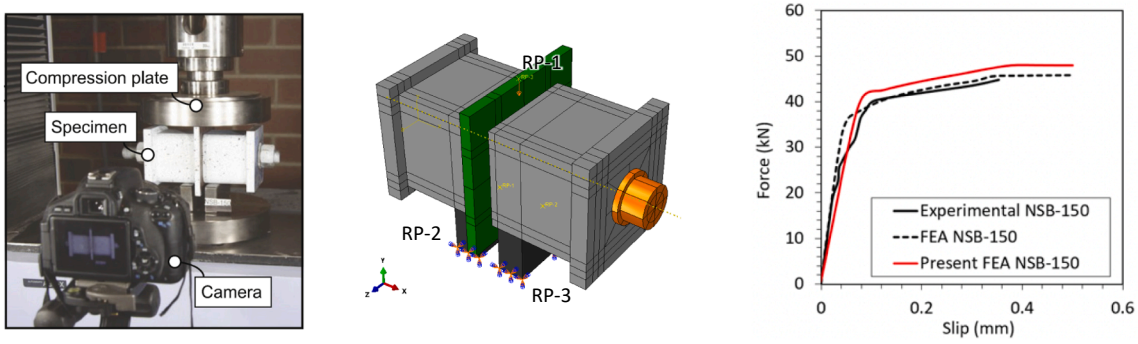

Fig. 11. FEA validation II.

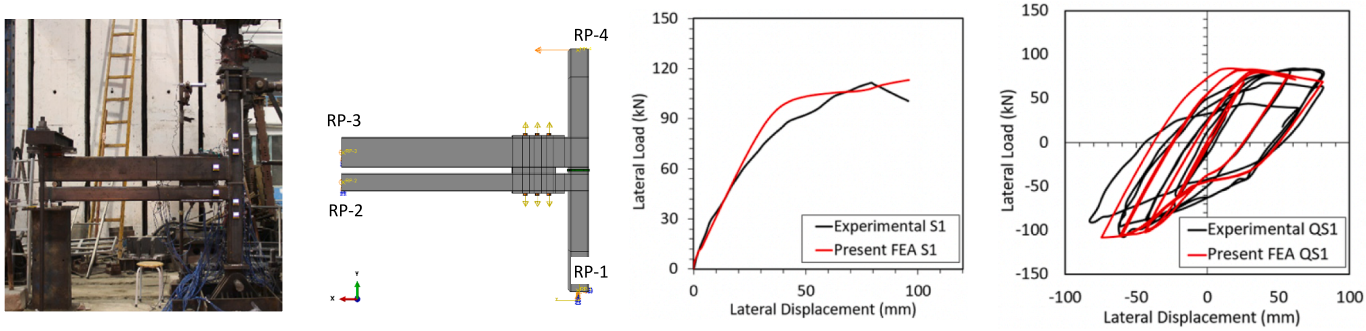

Fig. 12. FEA validation III.

force–displacement curves indicate a good agreement between the experimental and numerical results. The slight difference in the initial stiffness is attributed to the contribution to the shear resistance provided by the faying surfaces which are modelled through varying combinations of friction coefficients and elastic slip factors and thus cannot fully capture the condition and potential imperfections of the steel surfaces. Nevertheless, the slip loads and slip stages are predicted with great precision, supporting the overall reliability of the results. FEA validation III is based on the IMC studied by Chen et al. [92], illustrated in Fig. 12. The comparison of the monotonic and cyclic lateral load – displacement curves support the accuracy of the present FEA models and their experimental counterparts. The minor deviations are justified by the modelling simplifications of the experimental setups.

FEA validation of the calibrated high-damping rubber material

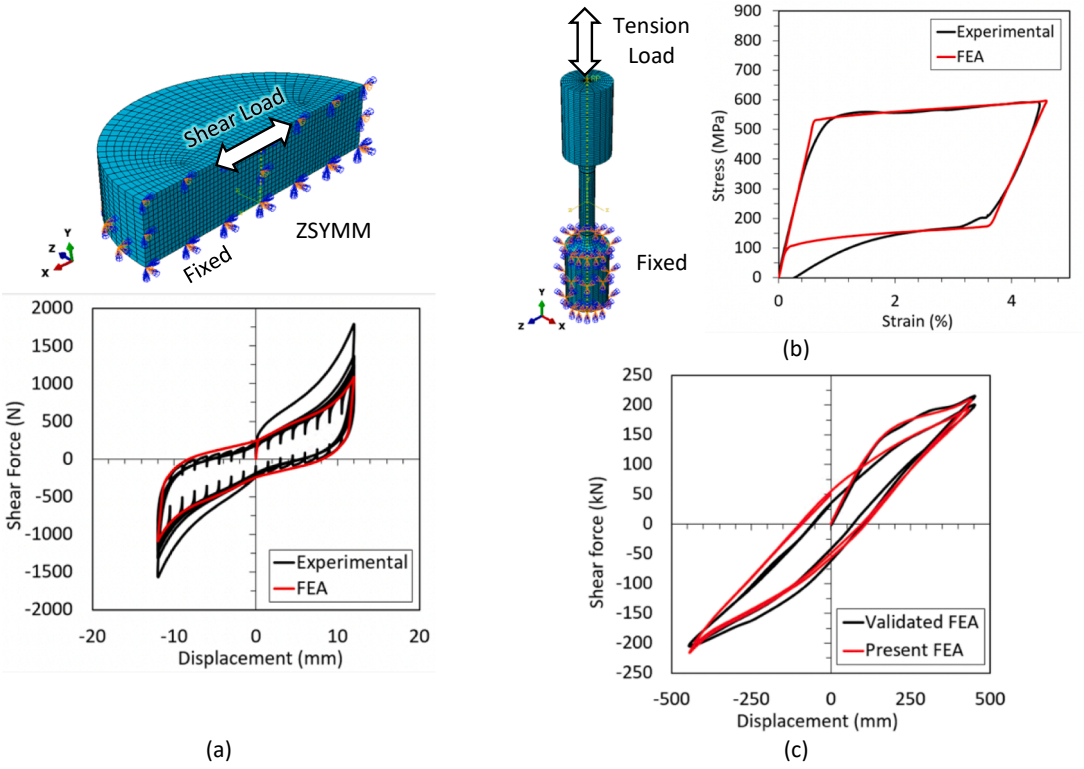

Fig. 13. Material model validations: (a) BB-Yeoh model, (b) supereleastic SMA model, (c) laminated elastomeric bearing model.

model is presented in Fig. 13 (a). The simple shear loading mode occurring in the double bonded shear (DBS) test setup has been imposed on a single cylindrical rubber strip by fixing the bottom surface and applying two cycles of up to + 200% shear strain (12 mm horizontal displacement) at the top by means of a reference point connected to the top surface through kinematic coupling activating all available DOFs. Taking advantage of the symmetric configuration of the DBS test, only half of the cylindrical rubber strip has been modelled, applying symmetrical boundary conditions for the other half. A qualitative interpretation of test results seen in Fig. 13 (a) demonstrates that the calibrated BB-Yeoh model is highly efficient in fully capturing the stabilised nonlinear large-strain behaviour, hysteresis and energy dissipation manifested during the cyclic loading of the HDR.

FEA validation of the calibrated SMA material model is shown in Fig. 13 (b). The loading conditions of the cyclic uniaxial tension test are imposed on the coupon by fixing the bottom gripped end and applying a cyclic displacement based on the desired strain amplitude by means of a reference point connected to the surface of the top gripped end through kinematic coupling. The stress–strain response simulated using the extracted material parameters for the superelastic model shows a good match with the experimental data.

Further supporting the FE modelling technique of the rubber bearing connector in the proposed inter-module connection, a numerical model has been developed based on the rubber isolator studied by Rahnavard and Thomas [93]. The bearing is loaded with two cycles of ±450 mm shear displacement (equivalent to 375% shear strain) under 2 MPa compressive stress. As shown in Fig. 13 (c) , the hysteretic behaviours predicted by the present FEA closely match the validated numerical

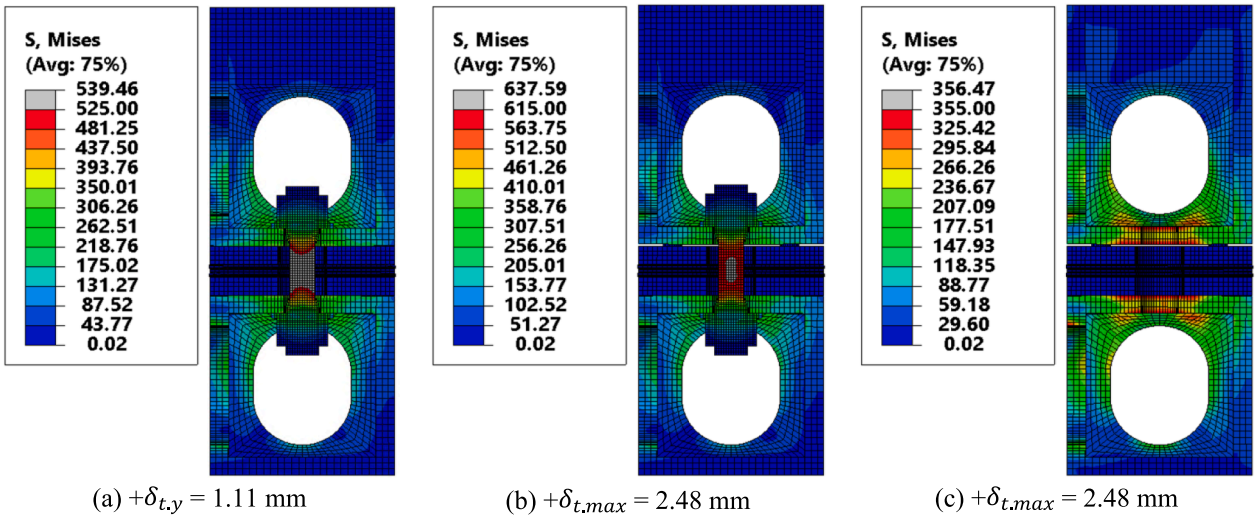

(a) $+\delta_{t.y} = 1.11$ mm (b) $+\delta_{t.max} = 2.48$ mm (c) $+\delta_{t.max} = 2.48$ mm

Fig. 14. Mises stress plots at yield and peak tensile displacement levels.

models from the literature in terms of initial stiffness and shear capacities in both positive and negative loading stages. Errors less than 5% are recorded, while the overall shape of the hysteretic curves in the present FEA model are in good agreement with those from the comparison data, proving that the current numerical model captured the structural behaviour and working mechanism of the rubber isolator with adequate precision.

All things considered, the results from this validation study demonstrate the high accuracy of the present FEA modelling techniques, further supporting their use for predicting the mechanical behaviour of the proposed hybrid IMC.

4. FEA results

4.1. Tension behaviour of the hybrid IMC

4.1.1. Deformation modes and stress states

To study the main deformation mode of the hybrid IMC under tensile axial load, specimen P50-E15 has been chosen as representative for the working mechanism of all specimens. As the bolt preload, $F_{p,C}$, is applied, it causes an initial compressive displacement in the elastomer layers of the HDR core, governed by the compressive stiffness of the rubber compound. This compressive displacement is considered when interpreting the results by calibrating the point of zero displacement at the start of the subsequent tension loading stages.

The stress contour in Fig. 14 (a) shows the Mises stress in the bolt's shank, corresponding to the start of "yield"-like point, just as the stress overcomes the forward transformation start stress, $\sigma_{Ms} = 525$ MPa. As the applied tensile displacement increases (Fig. 14 (b)), the inelastic stress concentrates uniformly in the bolt's shank, up to the ultimate/maximum point corresponding to the stress contours in the SMA bolt 's shank reaching the forward transformation finish stress $\sigma_{Mf} = 615$ MPa. Fig. 14 (c) shows the Mises plots limited by the yield strength of S355 steel, $f_y = 355$ MPa, indicating stress concentrations near bolt holes in the steel endplates of corner fittings, while the actual values barely exceed the yield limit. These results indicate that the hybrid IMC achieves the desired working mechanism in tension, as the tensile axial loading is mainly resisted by the SMA bolt, while the contribution of the endplates bending remains negligible.

This observation is further supported by the equivalent plastic strain (PEEQ) contours in Fig. 15, in which the non-zero values represent regions where the steel has sustained plastic deformation. The figures reveal that the plastic regions at the end of the third cycle of maximum tensile loading are localised towards the inner sides of the IMC, at interface between endplates and the outer plates of the HDR core, caused by the sudden section change as part of the endplates near bolt hole rims cantilever over the larger hole in the HDR core. While the overall values of PEEQ are reasonably low for all six tested specimens, the comparison between contours in Fig. 15 shows that increasing the endplate thickness, t_{cfe},reduces the inelastic deformations in corner fittings to insignificant values regardless of the level of bolt preload. Hence, in case of IMCs prone to experience tension loading due to uplift,

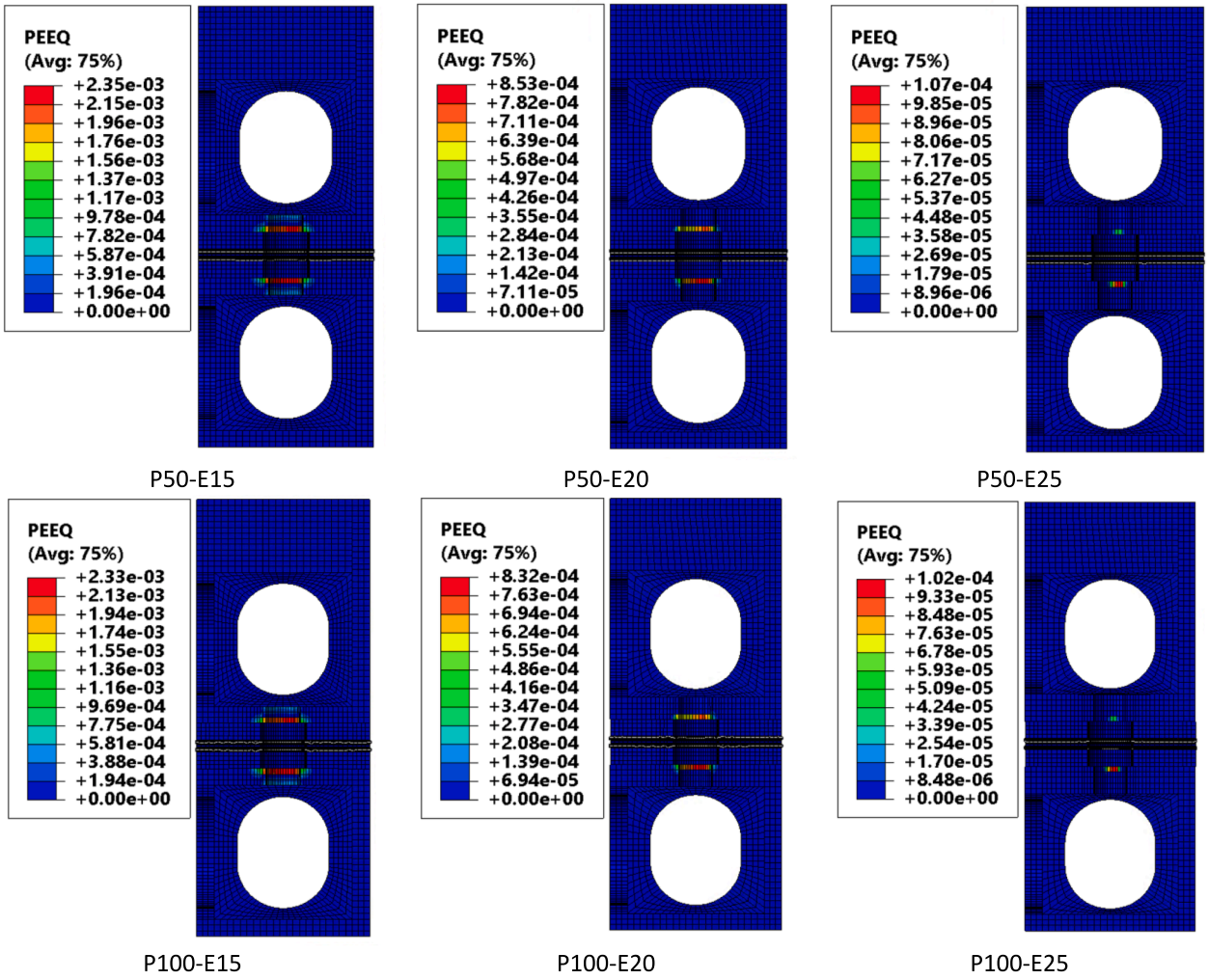

Fig. 15. Tension FEA: Equivalent plastic strain contours at end of third cycle of $+\delta/\delta_{max} = 1$.

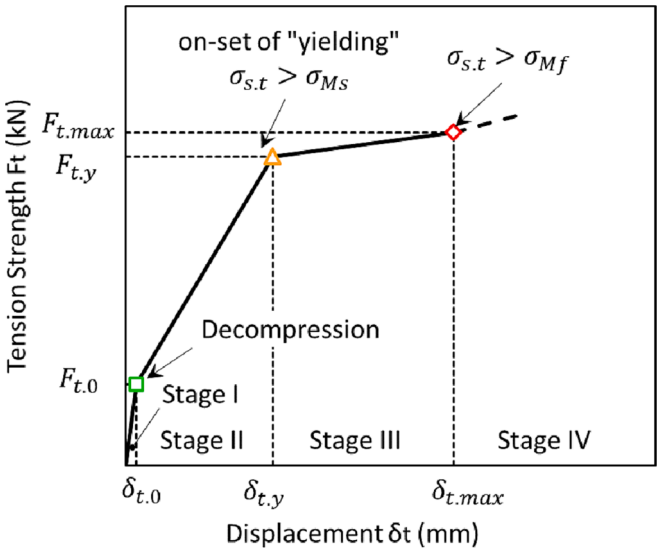

Fig. 16. Tension behaviour of hybrid IMC.

the corner fittings' endplates need to be provided with adequate thickness to ensure that the energy dissipated by the hybrid IMC during cyclic tensile axial loading is mostly provided by the pseudoelastic stress–-strain response of the SMA bolts without damaging the module's corner fittings.

4.1.2. Force-displacement curves

The tension behaviour of the hybrid IMC comprises four characteristic stages (Fig. 16) governed by key changes in the stress–strain response of the SMA bolt. Stage I (green square) represents the initial decompression of the preloaded bolt ($F_{t.0}, \delta_{t.0}$) and is characterised by a high initial stiffness, k_I, that depends on the preload level and the elastic modulus of austenite. As the tensile axial load increases, a slight stiffness degradation is observed during Stage II (orange triangle), described by k_{II} which depends mostly on the elastic modulus of austenite. Stage III (red diamond) represents the beginning of the transition from austenite to martensite marked by the onset of the 'yield-like' pseudoelastic plateau ($F_{t.y}, \delta_{t.y}$) and is characterised by a low stiffness, k_{III}, until the maximum tension strength and displacement ($F_{t.max}, \delta_{t.max}$) are achieved at the start of Stage IV when the transition to martensite is complete and indicating a slight hardening effect as the stress state in the bolt continues to develop towards the onset of plastic deformation. Since stress state beyond the martensite transformation point equates to the development of permanent inelastic strains in the SMA, it is desired to keep the mechanical response of the connection within the first three stages to maintain the re-centring effect under tension loading and the post-load demountability of the hybrid IMC. For this reason, the present study is only concerned with the mechanical behaviour of the IMC during the first three stages. The overall shape and stages that characterise the force–displacement behaviour of the hybrid IMC in tension are in good agreement with previous findings reported in the literature [63,81,86].

The comparison of hysteresis loops between the hybrid IMC specimens subjected to cyclic tensile axial loading is illustrated in Fig. 17. The blue dashed curve represents the initial monotonic loading performed to determine the maximum displacement used for tailoring the cyclic loading protocols for each of the tested specimens. The black dotted line indicates the "yield-like" tension strength of the SMA bolt predicted analytically using expression (18), confirming that the main yield mechanism of the hybrid IMC in tension is controlled by the forward transformation start stress, σ_{Ms}.

$$F_{t.y.pred} = A_s \sigma_{Ms} \tag{18}$$

Where A_s = the cross-sectional area of the bolt's shank and σ_{Ms} = the forward transformation start stress of SMA. The stage limits defined in Fig. 16 are also shown, while the corresponding values for tensile

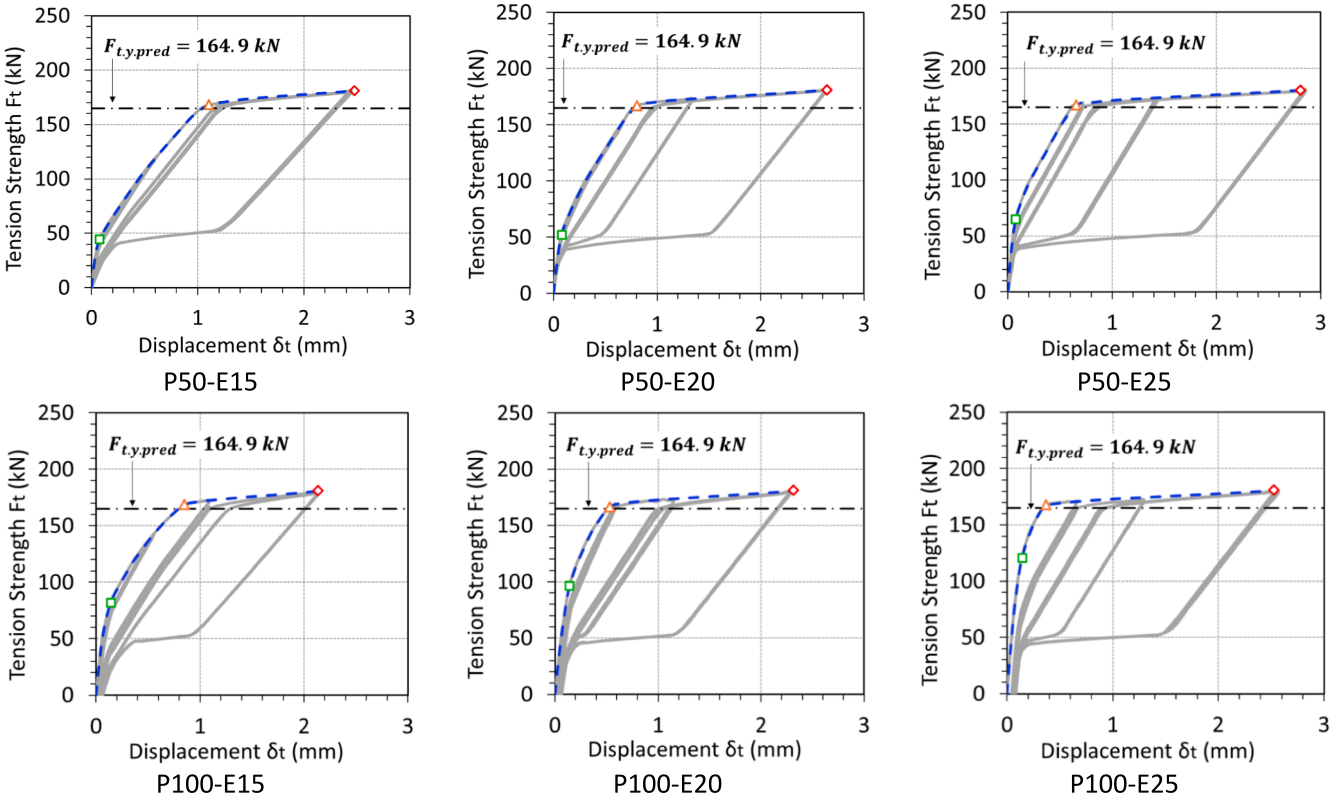

Fig. 17. Hysteresis loops for cyclic tensile axial loading.

Table 6
Mechanical parameters for monotonic tension FEA.

Specimen ID	$F_{t.0}$ (kN)	$\delta_{t.0}$ (mm)	k_I (kN/mm)	$F_{t.y}$ (kN)	$\delta_{t.y}$ (mm)	k_{II} (kN/mm)	$F_{t.max}$ (kN)	$\delta_{t.max}$ (mm)	k_{III} (kN/mm)	μ (-)
P50-E15	44.27	0.08	610.44	168.05	1.11	119.80	181.07	2.48	9.50	2.24
P50-E20	51.96	0.08	679.76	166.94	0.81	157.31	180.92	2.64	7.62	3.27
P50-E25	64.77	0.08	843.86	166.76	0.66	175.71	180.10	2.81	6.21	4.27
P100-E15	81.69	0.14	580.25	168.51	0.85	122.46	180.70	2.14	9.47	2.51
P100-E20	96.14	0.14	676.96	166.44	0.53	180.02	181.06	2.32	8.19	4.35
P100-E25	120.52	0.14	840.45	167.68	0.37	207.56	180.66	2.53	6.02	6.82

strength and displacement are given in Table 6.

In this regard, it can be observed that the analytical formula predicts the 'yield-like' strength, $F_{t.y}$, with reasonable accuracy for all tested specimens (max. 2.1% error), supporting the use of the analytical method as a preliminary measure of the expected results when designing the hybrid IMC for tension. Moreover, the difference of less than 2% between values of $F_{t.y}$ reported in Table 6 reveals that the influence of the chosen design parameters on the expected yield strength is negligible as long as the same bolt diameter is adopted, further confirming the SMA bolt is the main contributor to the tensile strength of the proposed IMC.

The evolution of the hysteresis loops shows that with each cycle of increasing loading amplitude (0.25 to 1 × δ/δ_{max}), the decompression strength ($F_{t.0}$) decreases, causing the second stiffness (k_{II}) to progressively degrade. While this effect is less pronounced for specimens P50-E15, P50-E20, and P50-E25, it becomes more noticeable in specimens P100-E15, P100-E20, and P100-E25. These results indicate that while lower bolt preload provides less stiffness in the initial loading cycle, it is generally more stable in subsequent cycles, while the higher stiffness supplied by the large bolt preload degrades to a larger extent, further suggesting that the effect of higher initial stiffness provided by the larger bolt preload is only relevant during the initial loading cycles and should not be counted for at later stages.

The ductility factor, μ, is a dimensionless ratio expressed by the normalisation of the maximum displacement, $\delta_{t.max}$, relative to the "yield-like" displacement, $\delta_{t.y}$ [94]. In the present study, μ has been determined using data from the initial monotonic loading representative of the first loading cycle up to peak displacement, $\delta_{t.max}$. As seen in in Fig. 17 and Table 6 all IMC specimens achieve reasonable ductility (μ >2), while the best results are present in specimens P50-E25 and P100-E25, highlighting the favourable effect of the thicker endplates. Generally, the higher initial stiffness provided in specimens with a high bolt preload (P100-E15, P100-E20, and P100-E25) causes a much smaller yield displacement, without the same impact on the peak displacement, which translates to larger ductility for specimens preloaded up to the forward transformation start stress. Nevertheless, it is important to note that the specimens preloaded only up to half the forward transformation start stress (P50-E15, P50-E20, and P50-E25) benefit from larger peak displacement capacities due to the lower initial stress levels in the bolt's shank. This effect equates to larger ductility factors available during latter loading cycles since the initial stiffness and the yield displacement in these specimens are less prone to degradation than their high bolt preload counterparts.

4.1.3. Energy dissipation and damping

The flag-shaped loops in Fig. 17 are a good first qualitative measure of the hybrid IMC's good energy dissipation capacity due to the transformation-induced pseudoelastic deformations in the SMA bolt, while a self-centring effect with limited residual displacements is present. Since the SMA bolt exhibits inherent energy dissipation capacity (EDC) and damping, it is of interest to further quantify these mechanical properties as illustrated in Fig. 18, based on data corresponding to the third cycle of each load amplitude.

The energy dissipated per cycle due to hysteresis, E_D, is defined as the area enclosed by the hysteresis loop, while the cumulative E_D, is the total level of energy dissipated up and including the current cycle. Fig. 18 shows that for all specimens, E_D increases with increasing load amplitude, while the energy dissipated during the third $\delta/\delta_{max} = 1$ cycle more than doubles compared to the previous load amplitude. The graph also indicates a better performance in terms of E_D per cycle for specimens

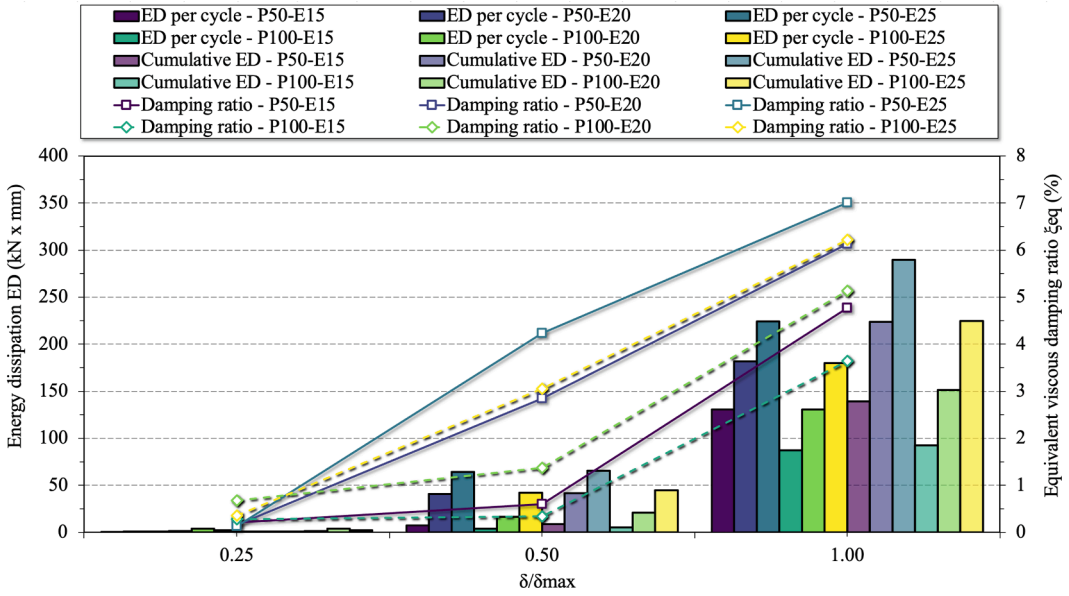

Fig. 18. Tension FEA: Energy dissipation/cycle, cumulative energy dissipation and equivalent viscous damping ratio.

with lower preloads (P50-E15, P50-E20, and P50-E25), regardless of the endplate thickness, which is in close agreement with the previous observation regarding the enhanced ductility available for these specimens during subsequent load cycles when compared to specimens with higher bolt preloads. As E_D per cycle is negligible during the low amplitude load cycles, the cumulative E_D registered in the high amplitude cycle is not substantially larger than the corresponding E_D per cycle, suggesting that the hybrid IMC is not very effective in dissipating energy during low amplitude tensile loading, with the major effect occurring during displacement levels equal to at least the maximum tensile displacement.

The equivalent viscous damping ratio, ξ_{eq}, is an alternative, dimensionless measure of the energy dissipation properties of the hybrid IMC, accounting for all energy dissipation mechanisms present during the cyclic loading [94] and is determined using expression (19)

$$\xi_{eq} = \frac{1}{4\pi}\frac{E_D}{E_{So}} \tag{19}$$

Where E_D = the energy dissipated in a cycle andE_{So} = maximum strain energy of an equivalent linear system. Data plotted in Fig. 18 reveals that all specimens exhibit reasonable levels of damping ranging from 3.57% for P100-E15 up to 7% for P50-E25 during the high amplitude load cycle. Once again, the unfavourable effect of high bolt preload is highlighted by the poorer damping properties of specimens P100-E15, P100-E20, and P100-E25 compared to their less preloaded counterparts. Moreover, it is observed that increasing the endplate thickness can greatly improve the damping capacity during the third $\delta/\delta_{max} = 0.5$ cycle, implying that as the hybrid IMC's tension behaviour is governed more by the SMA bolt and less by the bending of the endplates, the SMA bolt also contributes more efficiently to the overall damping capacity of the connection.

4.1.4. Effect of bolt preload and corner fitting endplates thickness

To qualitatively highlight the effect of the initial bolt preload and corner fitting endplates thickness on the tension behaviour of the hybrid IMC, the load–displacement curves under monotonic tension loading are illustrated in Fig. 19 (a) and (b), showing that a higher preload increases the decompression strength, $F_{t.0}$, while thicker endplates improve k_{II}, regardless of the level of bolt preload. The interaction graph in Fig. 19 (c) shows that the influence of preload is small and almost the same for both endplate thicknesses of 15 mm and 20 mm as the two lines are virtually parallel, while it is significantly different for an endplate thickness of 25 mm, suggesting that there is a strong interaction between bolt preload and endplate thickness at this level.

4.2. Combined compression and shear behaviour

4.2.1. Deformation modes and stress states

Taking N05-P50-VL1 as representative for all combined compression-shear specimens, the main deformation modes and stress states are shown in Fig. 20, to study the working mechanism of the hybrid IMC. Fig. 20 (a) shows the Mises stress in the hybrid IMC when the shear displacement reaches the onset of slipping, $\delta_{s.os}$. At this point, the initial gap of 1.5 mm due to the 3 mm bolt hole clearance provided in the corner fittings is still unchanged, while the two diagonally opposite shank regions which exceeded the forward transformation start stress, $\sigma_{Ms} = 525MPa$, are a sign of the bolt's main deformation mode defined as combined bending and shear. As the shear displacement increases and the bolt begins to slide, closing the clearance gap (Fig. 20 (b)), the stress in the bolt shank decreases below σ_{Ms}. At this stage the end of slipping displacement, $\delta_{s.es}$, is reached as the bolt shank has come into full contact with the bolt hole walls in the corner fitting. Further loading beyond this point resumes the development of stress in the tension side of the shank up until the forward transformation finish stress, σ_{Mf}, is eventually exceeded at the peak shear displacement, $\delta_{s.max}$ (Fig. 20 (c)). As explained in the case of pure tension loading, the hybrid IMC is intended to work only within the pseudoelastic limits of the SMA bolt, hence σ_{Mf} governs the ultimate limit of the mechanical behaviour during combined compression-shear loading as well. Overall, the stress evolution indicates that the hybrid IMC achieves the desired working mechanism in combined compression-shear, as the stress mainly develops in the SMA pin by virtue of the HDR core's flexibility in shear which prevents the direct bearing of corner fittings, keeping the stress levels in the module members negligible.

The equivalent plastic strain (PEEQ) contours illustrated in Fig. 21 reveal that the plastic regions at the end of the third cycle of peak shear displacement are localised around the rims of the bolt holes in the corner fitting endplates, and are caused by the high contact pressure that acts repetitively upon these surfaces as the SMA pin slides from side to side during cyclic shear loading. The comparison in Fig. 21 shows that increasing both the bolt preload and the depth of elastomer in the HDR cores has a favourable effect on the inelastic deformations in corner fittings, reflected by "P100-VL2" specimens with zero plastic strains, being most appropriate for achieving the desired reusability of the MBS frames.

4.2.2. Force-displacement curves

The combined compression-shear behaviour of the hybrid IMC is defined through four stages, as illustrated in Fig. 22 (a). Stage I (green square) represents the initial shear strength and stiffness up to the onset of slipping ($F_{s.os}, \delta_{s.os}$) and is characterised by a high initial stiffness, k_I, that depends on the bolt preload and the shear stiffness of the HDR core. Before the SMA pin starts slipping it is also noticed that the stress reaches the forward transformation start stress, σ_{Ms}, in a small region of the shank, suggesting that the elastic modulus of austenite also contributes to the first branch of the shear behaviour. As the shear load increases, the friction resistance due to the initial preload is exceeded and the hybrid IMC enters Stage II (orange triangle), described by a negligible slipping stiffness, k_{II} until the end of slipping shear strength and displacement ($F_{s.es}$, $\delta_{s.es}$) are reached. In Stage III (red diamond) the

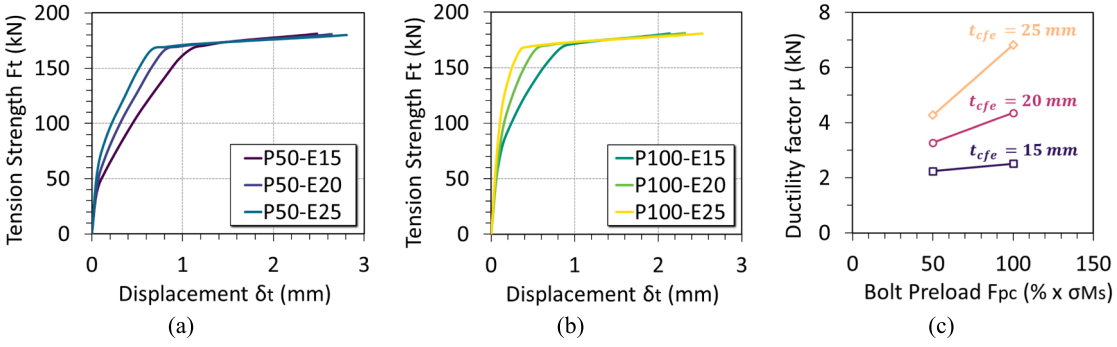

Fig. 19. Effect of bolt preload and endplate thickness on the mechanical response.

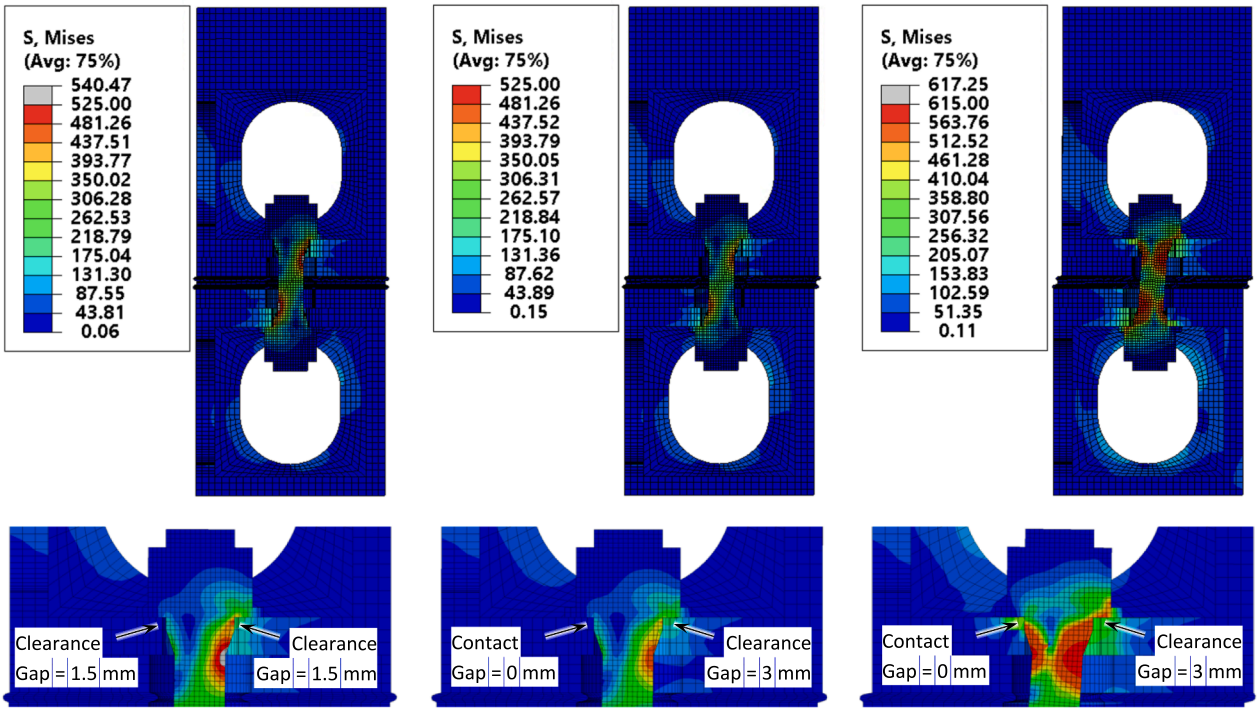

(a) $+\delta_{s,os} = 1.00$ mm (b) $+\delta_{s,es} = 3.75$ mm (c) $+\delta_{s,max} = 7.25$ mm

Fig. 20. Mises stress plots at: (a) onset of slipping, (b) end of slipping, and (c) peak shear displacement levels.

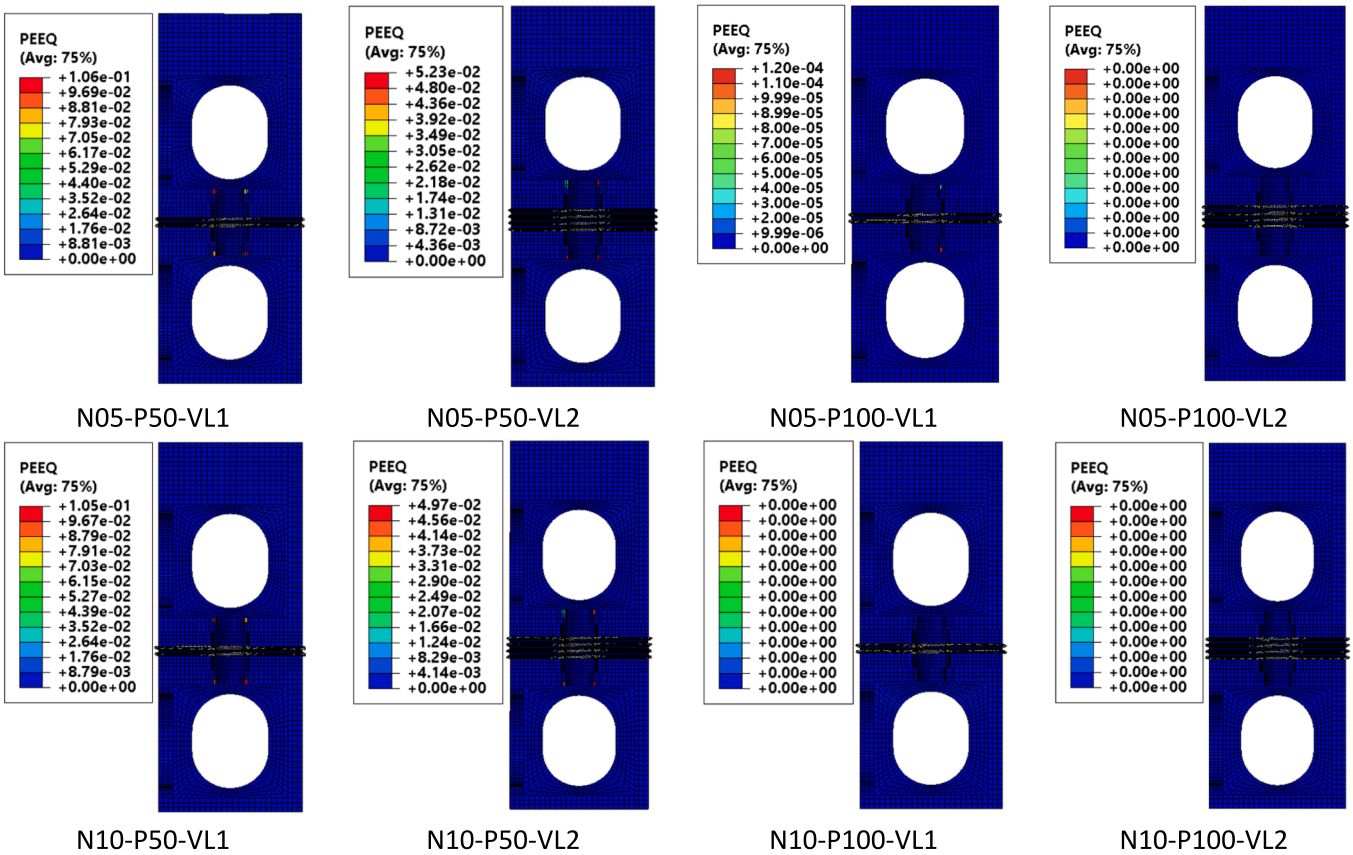

Fig. 21. Combined compression-shear FEA: Equivalent plastic strain contours at end of third cycle of $+\delta/\delta_{max} = 1$.

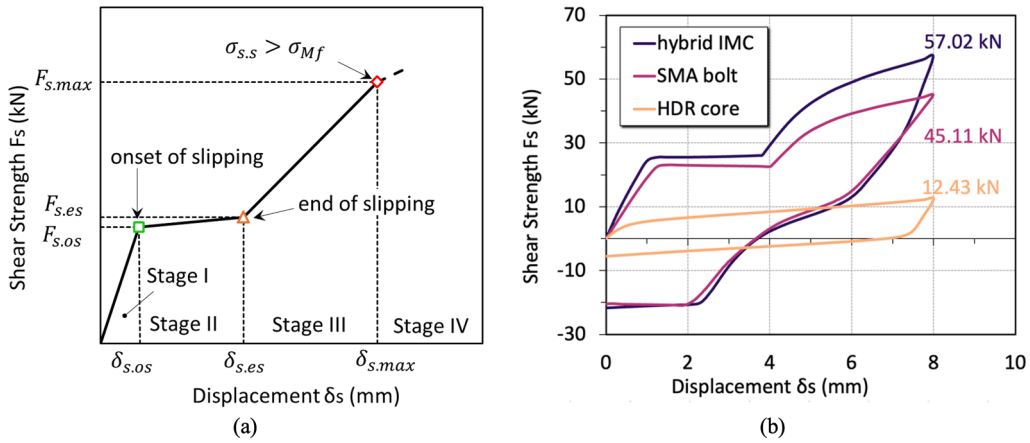

Fig. 22. Shear FEA: (a) generalized F-δ behaviour, (b) individual contribution of IMC components.

contact pressure between the SMA pin and the corner fitting's bolt hole walls increases, characterised by a lower stiffness, k_{III}, as the IMC approaches the peak shear strength and displacement ($F_{s.max}$, $\delta_{s.max}$). As defined for the tension behaviour, Stage IV reaches beyond the upper limit of the pseudoelastic response in the SMA pin and is considered outside of the safe working mechanism intended for the proposed design.

Fig. 22 (b) shows the force contribution of the SMA bolt and HDR core when loaded up to a shear displacement of + 8 mm, while the corresponding maximum shear strengths of each component, F_{SMA} = 45.11 kN, F_{HDR} = 12.43 kN, are in good agreement with the total F_{IMC} = 57.02 kN (error less than 1%). From the graph, it is confirmed that in the current design the SMA pin provides the major contribution to the total shear response of the hybrid IMC (i.e., 79.1%) while the HDR core plays a secondary role. In terms of available EDC, it is also observed from the size and shape of the hysteresis loops that the SMA bolt is the main contributor, while the HDR core's impact on energy dissipation is most effective after the end of the initial slipping stage. Another noteworthy observation is that the HDR core's hysteresis does not affect the overall self-centring effect of the hybrid IMC, which remains governed by the SMA bolt alone, confirming the favourable hybrid working mechanism expected from the IMC.

To facilitate the qualitative and quantitative assessment of the cyclic shear response of the hybrid IMC, the hysteresis loops are plotted in Fig. 23 and corresponding mechanical parameters are extracted in Table 7. While IMCs with higher bolt preloads ("P100" specimens) generally achieve larger onset of slipping strengths ($F_{s.os}$), the initial stiffness branches are weaker than those of IMCs with lower bolt preloads ("P50" specimens), which is further confirmed by the higher k_I values in "P50" specimens. The larger friction resistance due to higher bolt preloads in "P100" specimens delays the slipping stage, which is highlighted by the onset of slipping displacements, $\delta_{s.os}$, that are generally larger in these specimens. It is also noteworthy that while the shorter HDR cores ("VL1" specimens) generally deliver better shear strength and stiffness during the first and third stages (k_I and k_{III}), at the expense of lower deformation capacity. This is further reflected by the peak shear displacements of $\delta_{s.max}$ = 7.25 mm achieved by "VL1" specimens, and $\delta_{s.max}$ = 8.25 mm for "VL2" specimens, corresponding to shear strain values in the HDR cores of γ = 90% and γ = 50% respectively (where γ is the percentage of applied shear displacement relative to the total height of elastomer layers). Consequently, IMCs with shorter HDR cores may cause the adjoining module frame members to attract larger seismic forces, contributing more radically to the overall joint resistance during lateral loading, and thus suffering more damage.

In the case of shear FEA, μ is expressed by the normalisation of the maximum displacement, $\delta_{s.max}$, relative to the onset of slipping displacement, $\delta_{s.os}$, which is regarded as an equivalent "yield"-like point on the *F-δ* curve. As before, ductility ratios are based on data from the initial monotonic loading cycle up to the maximum displacement, $\delta_{s.max}$ represented by the blue dash curves. Table 7 reveals that the best ductility ratios are achieved in specimens with lower preloads ("P50" specimens) due to the larger post end of slipping deformation capacities available as opposed to specimens with higher preloads ("P100" specimens), defined by much lower peak shear displacements. This is in contrast with the results reported in the tension behaviour, where larger preloads equated to better ductility ratios during the first loading cycles. It is also noted that there is virtually no difference in ductility ratios between specimens with different compressive axial loads applied ("N05" vs. "N10" specimens), highlighting the lack of influence of the gravitational loading on the deformation capacity of the hybrid IMC during combined compression-shear loading. Furthermore, it becomes clear that the IMCs with shorter and hence stiffer HDR cores in shear ("VL1" specimens) are generally more efficient in terms of ductility than their more flexible counterparts ("VL2" specimens).

4.2.3. Energy dissipation and damping

The hysteresis loops reported in Fig. 23 for the combined compression-shear FEA indicate reasonable EDC in all IMC specimens, marked by the round and "fat" shapes up to the end of slipping shear displacement, $\delta_{s.es}$. While the high preload "P100" specimens generally provide more robust hysteresis loops throughout each displacement amplitude cycle and up to the peak displacement, δ_{smax}, due to the higher initial strength and stiffness, the low preload "P50" specimens demonstrate comparable EDC due to the 'flap'-like region in the hysteresis loops present post $\delta_{s.es}$ as an effect of the larger deformation capacity available in the less stressed bolts.

These observations are further supported by data illustrated in Fig. 24, which highlights the favourable effect of higher preload in "P100" specimens in terms of energy dissipated during the third δ/δ_{max} = 1 cycle. While the effect is more pronounced in IMCs subjected to the lower axial load ("N05" specimens), the difference becomes marginal as the axial load also increases ("N10" specimens). The graph also indicates a better performance in terms of E_D per cycle for IMCs with shorter and stiffer HDR cores ("VL1" specimens), which is in close agreement with the previous observation regarding the enhanced ductility available for these specimens. The cumulative E_D registered in the high amplitude cycle is reasonably larger than the corresponding E_D per cycle, as it indicates that all tested hybrid IMCs are efficient in absorbing energy during lower amplitude shear loading cycles too, demonstrating a robust cyclic shear behaviour in terms of EDC.

Fig. 24 reveals that the highest damping ratios (up to 45%) are achieved during the third δ/δ_{max} = 0.5 cycle in IMCs with lower bolt preloads ("P50" specimens). Moreover, it is observed that "P50" specimens experience an abrupt decrease in damping capacity as the applied

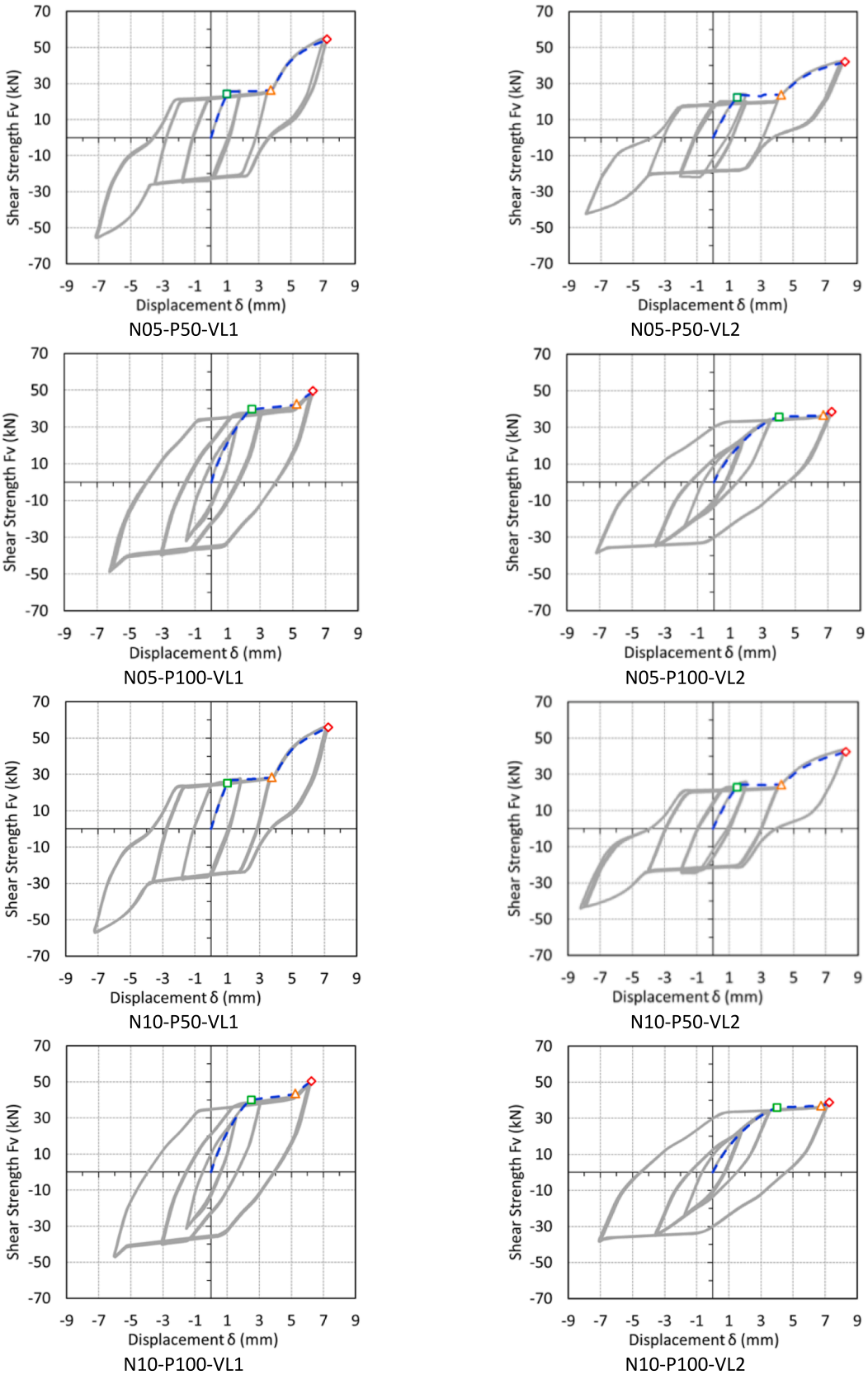

Fig. 23. Hysteresis loops for cyclic shear loading.

Table 7
Mechanical parameters for monotonic shear FEA.

Specimen ID	$F_{s.os}$ (kN)	$\delta_{s.os}$ (mm)	k_I (kN/mm)	$F_{s.es}$ (kN)	$\delta_{s.es}$ (mm)	k_{II} (kN/mm)	$F_{s.max}$ (kN)	$\delta_{s.max}$ (mm)	k_{III} (kN/mm)	μ (-)
N05-P50-VL1	24.25	1.00	24.25	26.27	3.75	0.73	54.43	7.25	8.05	7.25
N05-P50-VL2	22.36	1.50	14.90	23.68	4.26	0.48	42.05	8.26	4.59	5.51
N05-P100-VL1	39.62	2.50	15.85	42.55	5.25	1.07	49.43	6.25	6.87	2.50
N05-P100-VL2	35.74	4.00	8.93	36.59	6.75	0.31	38.47	7.25	3.75	1.81
N10-P50-VL1	25.21	1.00	25.21	28.33	3.75	1.13	55.83	7.27	7.82	7.27
N10-P50-VL2	22.89	1.50	15.26	24.24	4.26	0.49	42.35	8.26	4.53	5.51
N10-P100-VL1	40.06	2.50	16.02	43.38	5.25	1.21	50.43	6.25	7.06	2.50
N10-P100-VL2	35.93	4.00	8.98	36.81	6.75	0.32	38.61	7.26	3.54	1.81

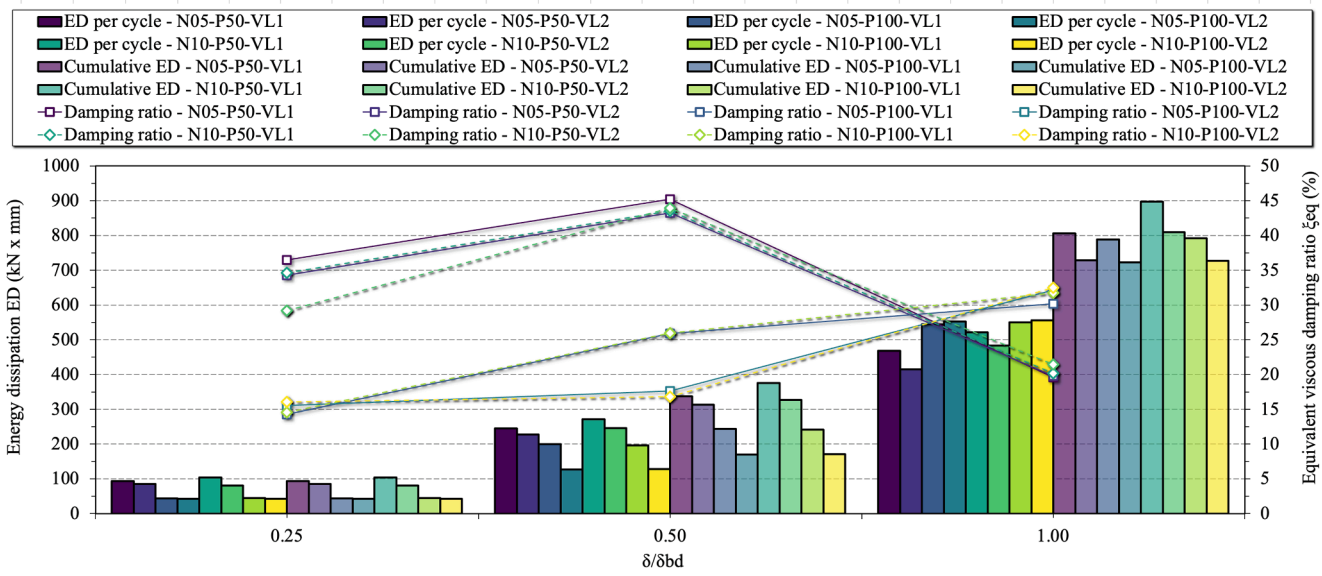

Fig. 24. Shear FEA: Energy dissipation/cycle, cumulative energy dissipation and equivalent viscous damping ratio.

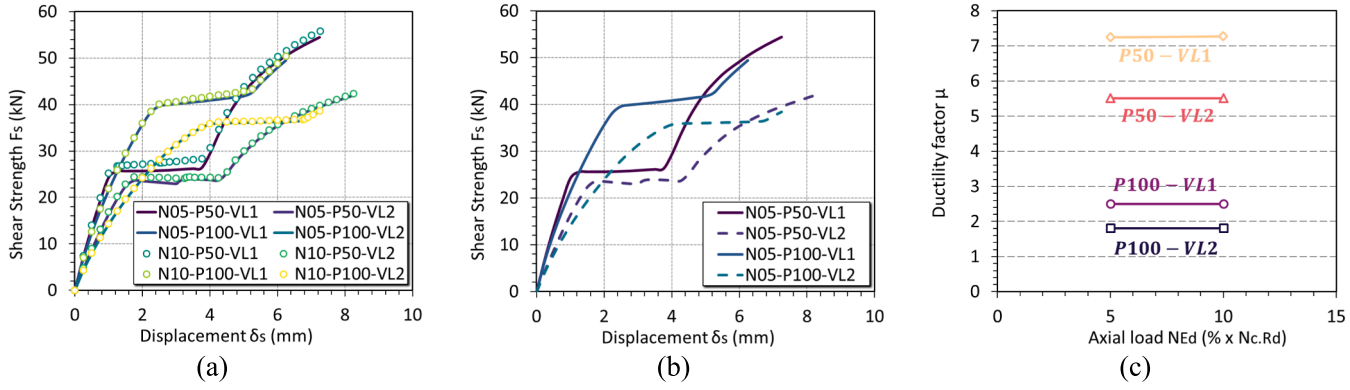

Fig. 25. Effect of axial load magnitude, bolt preload and HDR core vertical layout on the mechanical response.

shear displacement approaches the peak values (third '$\delta/\delta_{max} = 1$' cycle), reflected by the irregularity of the hysteresis loops too, while "P100" specimens follow a more constant upward trend achieving lower damping ratios during low amplitude cycles, but better overall performance at peak shear displacement. However, it is noteworthy that while "P50" specimens compromise on damping capacity at high amplitude cycles, they achieve much better recentring than IMCs with higher bolt preloads. Therefore, the impact of the bolt preload on EDC and damping achieved during cyclic shear loading need to be carefully considered, depending on the displacement amplitude for which the hybrid IMCs are to be designed for and the desired level of recoverable displacement.

4.2.4. Effect of compressive axial load magnitude, bolt preload and, vertical layout of HDR core

To qualitatively highlight the effect of the compression load, bolt preload and vertical layout of the HDR core on the shear behaviour of the hybrid IMC, the monotonic load–displacement curves for all tested connections are illustrated in Fig. 25. The dotted curves in Fig. 25 (a) indicated that the higher axial load has a negligible effect on the overall mechanical response regardless of the bolt preload or shear stiffness of the HDR core. This observation is further supported by the interaction graph in Fig. 25 (c), as the four lines are perfectly parallel. Furthermore, the favourable effect of preloading the bolts up to σ_{Ms} on the onset of

slipping strength, $F_{s.os}$, is highlighted in Fig. 25 (b), as the onset of slipping stage is delayed, yet at the expense of slightly weaker pre-slipping stiffness, k_1, and smaller maximum shear displacements.

5. Concluding remarks

In the present study a novel hybrid IMC employing a high-damping rubber (HDR) core and shape-memory alloy (SMA) bolt is proposed and its tension and combined compression-shear behaviours are studied and quantified by means of validated high-fidelity FEA modelling approaches in Abaqus®. Calibrated and validated material models using data from experimental material characterisation tests have facilitated the full characterisation of the hybrid mechanical response, determining the deformation modes, stress states, hysteresis loops and mechanical parameters. The parametric FEA included the variation of bolt preload, endplate thickness, axial load magnitude and the vertical layout of the HDR core. The study represents a preliminary investigation of the proposed IMC, serving as a proof-of-concept to give insight into its working mechanism. The key points are summarised as follows.

1. The hybrid IMC's tension behaviour is governed by the stress–strain response of the SMA pin and is divided into four separate load stages corresponding to transformation-induced stress changes suffered by the bolt. The "yield"-like tension capacity of the IMC can be analytically predicted with reasonable accuracy, giving a good preliminary measure for the elastic design of the connection. The IMC presents robust cyclic performance under tension loading, delivering good ductility, EDC and damping ratio combined with effective re-centring effects due to the pseudoelastic behaviour of the SMA bolt.
2. The studied parameters for tension FEA have revealed that providing sufficiently thick corner fitting endplates has a favourable effect on the initial strength and stiffness of the IMC, while also improving the overall ductility, EDC and damping due to a more efficient contribution of the SMA bolt to the IMC's tension behaviour. At the same time, preloading the SMA pin up to the forward transformation start stress improves the initial stiffness and overall ductility of the IMC, but has a negative impact on the EDC and damping during subsequent load cycles as the stiffness degrades more noticeably due to the higher initial stress in the bolt's shank.
3. The combined compression-shear behaviour of the proposed IMC relies on the effectiveness of the resilient HDR core to undergo large shear straining without failing, while the main resistance is provided by a combined shear-bending deformation state in the SMA pin's shank. The total shear response has been successfully decoupled, revealing the major contribution of the SMA bolt in terms of EDC and recoverable deformation, while the HDR core plays a supporting, yet critical role.
4. The parameters varied during combined compression-shear FEA have indicated that a deeper HDR core can have a more favourable effect on the lateral load resilience of the IMC as it delays the formation of plastic strains in the corner fittings, improving the module's reuse prospects. Moreover, the level of bolt preload applied has a significant impact on the ductility, EDC and damping of the IMC under cyclic shear, requiring careful consideration based on the intended deformation capacity. In addition, it has been found that while increasing the compressive axial load slightly improves the strength and stiffness of the IMC, the effect is mostly negligible within the range of magnitudes considered.
5. Overall, the study showcases the favourable cyclic performance of the proposed IMC under the main deformation modes expected in tall self-standing MBSs during lateral loading. Due to the effective contribution of each component to the combined hybrid response, the connection succeeds in preventing the formation of significant plastic damage in the MBS's corner fittings to facilitate reusability of modules, while the resilience and demountability of the IMC are ensured provided that the SMA pin is designed to work within the pseudoelastic domain.

In the near future, a meso-scale experimental campaign currently underway at City, University of London will be the subject of follow-up research. The meso-scale tests will focus on capturing the structural system behaviour including the influence of the beam-column joints (BCJs). The results can then be correlated to the present study to reverse engineer and fine-tune specific material properties at IMC level, while also advising on the development of accurate simplified joint models for analytical and global analysis models (macro-scale level).

Declaration of Competing Interest

The authors declare that they have no known competing financial interests or personal relationships that could have appeared to influence the work reported in this paper.

Data availability

No data was used for the research described in the article.

Acknowledgements

The authors would like to thank Mr Carmine Maletta, Professor of Machine Design at University of Calabria and CEO of 2SMArteST, and Mr Fabrizio Niccoli, Researcher at University of Calabria and CTO of 2SMArtEST for their very valuable and continuous technical support. Their experience and expertise have been instrumental to the material characterisation and fabrication of the pseudoelastic shape-memory alloy bolts. The authors would also like to thank Mr Hamid Ahmadi, Head of Division at TARRC, for his technical support with regards to the material characterisation and fabrication of high-damping rubber cores.

This was work is funded by The Leverhulme Trust and Royal Academy of Engineering [LTSRF1819_15_40], the Engineering and Physical Sciences Research Council [EP/L504993/1] and SC4 limited.

References

[1] Lawson RM, Ogden RG, Goodier C. Design in modular construction. Oxon: CRC Press; 2014.
[2] Liew JYR, Chua YS, Dai Z. Steel concrete composite systems for modular construction of high-rise buildings. Structures 2019;21:135–49. https://doi.org/10.1016/j.istruc.2019.02.010.
[3] Thai H-T, Ngo T, Uy B. A review on modular construction for high-rise buildings. Structures 2020;28:1265–90. https://doi.org/10.1016/j.istruc.2020.09.070.
[4] Annan CD, Youssef MA, El Naggar MH. Experimental evaluation of the seismic performance of modular steel-braced frames. Eng Struct 2009;31:1435–46. https://doi.org/10.1016/j.engstruct.2009.02.024.
[5] Fathieh A, Mercan O. Seismic evaluation of modular steel buildings. Eng Struct 2016;122:83–92. https://doi.org/10.1016/j.engstruct.2016.04.054.
[6] Gunawardena T, Ngo T, Mendis P. Behaviour of multi-storey prefabricated modular buildings under seismic loads. Earthquakes and Struct 2016;11:1061–76. https://doi.org/10.12989/eas.2016.11.6.1061.
[7] Srisangeerthanan S, Hashemi MJ, Rajeev P, Gad E, Fernando S. Numerical study on the effects of diaphragm stiffness and strength on the seismic response of multi-story modular buildings. Eng Struct 2018;163:25–37. https://doi.org/10.1016/j.engstruct.2018.02.048.
[8] Chua YS, Liew JYR, Pang SD. Modelling of connections and lateral behavior of high-rise modular steel buildings. J Constr Steel Res 2020;166. https://doi.org/10.1016/j.jcsr.2019.105901.
[9] Lacey AW, Chen W, Hao H, Bi K. Effect of inter-module connection stiffness on structural response of a modular steel building subjected to wind and earthquake load. Eng Struct 2020;213. https://doi.org/10.1016/j.engstruct.2020.110628.
[10] Wang Z, Tsavdaridis KD. Optimality criteria-based minimum-weight design method for modular building systems subjected to generalised stiffness constraints: a comparative study. Eng Struct 2022;251:113472. https://doi.org/10.1016/j.engstruct.2021.113472.
[11] Sendanayake SV, Thambiratnam DP, Perera NJ, Chan THT, Aghdamy S. Enhancing the lateral performance of modular buildings through innovative inter-modular connections. Structures 2021;29:167–84. https://doi.org/10.1016/j.istruc.2020.10.047.

[12] Deng E-F, Zong L, Ding Y, Dai X-M, Lou N, Chen Y. Monotonic and cyclic response of bolted connections with welded cover plate for modular steel construction. Eng Struct 2018;167:407–19. https://doi.org/10.1016/j.engstruct.2018.04.028.

[13] Lee S, Park J, Shon S, Kang C. Seismic performance evaluation of the ceiling-bracket-type modular joint with various bracket parameters. J Constr Steel Res 2018;150:298–325. https://doi.org/10.1016/j.jcsr.2018.08.008.

[14] Cho B-H, Lee J-S, Kim H, Kim D-J. Structural performance of a new blind-bolted frame modular beam-column connection under lateral loading. Appl Sci 2019;9. https://doi.org/10.3390/app9091929.

[15] Dai X-M, Zong L, Ding Y, Li Z-X. Experimental study on seismic behavior of a novel plug-in self-lock joint for modular steel construction. Eng Struct 2019;181:143–64. https://doi.org/10.1016/j.engstruct.2018.11.075.

[16] Lee J-S, Lee H-D, Shin K-J, Kim H-J, Lee K-M. Structural performance evaluation of modular connections using developed blocks. Int J Steel Struct 2021. https://doi.org/10.1007/s13296-021-00500-2.

[17] Chen Z, Liu J, Yu Y. Experimental study on interior connections in modular steel buildings. Eng Struct 2017;147:625–38. https://doi.org/10.1016/j.engstruct.2017.06.002.

[18] Sanches R, Mercan O, Roberts B. Experimental investigations of vertical post-tensioned connection for modular steel structures. Eng Struct 2018;175:776–89. https://doi.org/10.1016/j.engstruct.2018.08.049.

[19] Deng E-F, Zong L, Ding Y, Zhang Z, Zhang J-F, Shi F-W, et al. Seismic performance of mid-to-high rise modular steel construction - a critical review. Thin-Walled Struct 2020;155:106924. https://doi.org/10.1016/j.tws.2020.106924.

[20] Chen Z, Khan K, Khan A, Javed K, Liu J. Exploration of the multidirectional stability and response of prefabricated volumetric modular steel structures. J Constr Steel Res 2021;184. https://doi.org/10.1016/j.jcsr.2021.106826.

[21] Sultana P, Youssef MA. Seismic performance of modular steel-braced frames utilizing superelastic shape memory alloy bolts in the vertical module connections. J Earthq Eng 2018;24:628–52. https://doi.org/10.1080/13632469.2018.1453394.

[22] Wu CX, Yang Y, Wu CY, Yang T, Xu X. Research on seismic behaviour analysis of shock absorbing structure and connecting joints of container assembly structures. Steel Construction 2019;34:1-8+73.

[23] Jing J, Clifton GC, Roy K, Lim JBP. Seismic protection of modular buildings with bonded rubber unit sliders: experimental study. Thin-Walled Struct 2020;154. https://doi.org/10.1016/j.tws.2020.106790.

[24] Smith R, Merello R, Willford M. Intrinsic and supplementary damping in tall buildings. Proceedings of the Institution of Civil Engineers - Structures and Buildings 2010;163:111-8. Doi: 10.1680/stbu.2010.163.2.111.

[25] Bergstrom JS, Boyce MC. Constitutive modeling of the large strain time-dependent behavior of elastomers. J Mech Phys Solids 1998;46:931–54.

[26] Dall'Asta A, Ragni L. Experimental tests and analytical model of high damping rubber dissipating devices. Eng Struct 2006;28:1874–84. https://doi.org/10.1016/j.engstruct.2006.03.025.

[27] Sheikhi J, Fathi M, Rahnavard R. Natural rubber bearing incorporated with high toughness steel ring dampers. Structures 2020;24:107–23. https://doi.org/10.1016/j.istruc.2020.01.013.

[28] Rahnavard R, Rebelo C, Craveiro HD, Napolitano R. Numerical investigation of the cyclic performance of reinforced concrete frames equipped with a combination of a rubber core and a U-shaped metallic damper. Eng Struct 2020;225:111307. https://doi.org/10.1016/j.engstruct.2020.111307.

[29] Ragni L, Dezi L, Dall'Asta A, Leoni G. HDR devices for the seismic protection of frame structures: Experimental results and numerical simulations. Earthquake Engng Struct Dyn 2009;38:1199–217. https://doi.org/10.1002/eqe.891.

[30] Zhou Y, Shi F, Ozbulut OE, Xu H, Zi D. Experimental characterization and analytical modeling of a large-capacity high-damping rubber damper. Struct Control Health Monit 2018;25:1–17. https://doi.org/10.1002/stc.2183.

[31] Chen Y, Chen C, Ma Q, Jiang H, Wan Z. Study on mechanical properties of high damping viscoelastic dampers. Adv Struct Eng 2019;22:2925–36. https://doi.org/10.1177/1369433219853440.

[32] Burtscher SL, Dorfmann A. Compression and shear tests of anisotropic high damping rubber bearings. Eng Struct 2004;26:1979–91. https://doi.org/10.1016/j.engstruct.2004.07.014.

[33] Wei W, Tan P, Yuan Y, Zhu H. Experimental and analytical investigation of the influence of compressive load on rate-dependent high-damping rubber bearings. Constr Build Mater 2019;200:26–35. https://doi.org/10.1016/j.conbuildmat.2018.12.086.

[34] Zhang Y, Li J. Effect of material characteristics of high damping rubber bearings on aseismic behaviors of a two-span simply supported beam bridge. Adv Mater Sci Eng 2020:1–8. https://doi.org/10.1155/2020/9231382.

[35] Fang C, Wang W. Shape memory alloys for seismic resilience. Singapore: Springer Nature Singapore Pte Ltd.; 2020.

[36] Lagoudas DC. Shape Memory Alloys - Modeling and Engineering Applications. vol. 1. Boston, MA: Springer US; 2008. Doi: 10.1007/978-0-387-47685-8.

[37] Abavisani I, Rezaifar O, Kheyroddin A. Multifunctional properties of shape memory materials in civil engineering applications: a state-of-the-art review. J Build Eng 2021;44:102657. https://doi.org/10.1016/j.jobe.2021.102657.

[38] Desroches R, Smith B. Shape memory alloys in seismic resistant design and retrofit: a critical review of their potential and limitations. J Earthq Eng 2008;8:415–29. https://doi.org/10.1080/13632460409350495.

[39] Zareie S, Issa AS, Seethaler RJ, Zabihollah A. Recent advances in the applications of shape memory alloys in civil infrastructures: a review. Structures 2020;27:1535–50. https://doi.org/10.1016/j.istruc.2020.05.058.

[40] Wilde K, Gardoni P, Fujino Y. Base isolation system with shape memory alloy device for elevated highway bridges. Eng Struct 2000;22:222–9. https://doi.org/10.1016/S0141-0296(98)00097-2.

[41] Choi E, Nam TH, Oh JT, Cho BS. An isolation bearing for highway bridges using shape memory alloys. Mater Sci Eng A 2006;438–440:1081–4. https://doi.org/10.1016/j.msea.2006.05.098.

[42] Sharabash AM, Andrawes BO. Application of shape memory alloy dampers in the seismic control of cable-stayed bridges. Eng Struct 2009;31:607–16. https://doi.org/10.1016/j.engstruct.2008.11.007.

[43] Rahman Bhuiyan A, Alam MS. Seismic performance assessment of highway bridges equipped with superelastic shape memory alloy-based laminated rubber isolation bearing. Eng Struct 2013;49:396–407. https://doi.org/10.1016/j.engstruct.2012.11.022.

[44] Gur S, Mishra SK, Chakraborty S. Performance assessment of buildings isolated by shape-memory-alloy rubber bearing: comparison with elastomeric bearing under near-fault earthquakes: SHAPE-MEMORY-ALLOY RUBBER BEARING FOR BASE ISOLATION. Struct Control Health Monit 2014;21:449–65. https://doi.org/10.1002/stc.1576.

[45] Shinozuka M, Chaudhuri SR, Mishra SK. Shape-Memory-Alloy supplemented Lead Rubber Bearing (SMA-LRB) for seismic isolation. Probab Eng Mech 2015;41:34–45. https://doi.org/10.1016/j.probengmech.2015.04.004.

[46] Casagrande L, Villa E, Nespoli A, Occhiuzzi A, Bonati A, Auricchio F. Innovative dampers as floor isolation systems for seismically-retrofit multi-storey critical facilities. Eng Struct 2019:201. https://doi.org/10.1016/j.engstruct.2019.109772.

[47] Sheikhi J, Fathi M, Rahnavard R, Napolitano R. Numerical analysis of natural rubber bearing equipped with steel and shape memory alloys dampers. Structures 2021;32:1839–55. https://doi.org/10.1016/j.istruc.2021.03.115.

[48] Fang C, Liang D, Zheng Y, Lu S. Seismic performance of bridges with novel SMA cable-restrained high damping rubber bearings against near-fault ground motions. Earthquake Engng Struct Dyn 2022;51:44–65. https://doi.org/10.1002/eqe.3555.

[49] Corfar D-A, Tsavdaridis KD. A comprehensive review and classification of inter-module connections for hot-rolled steel modular building systems. J Build Eng 2022;50:104006. https://doi.org/10.1016/j.jobe.2022.104006.

[50] Chen Z, Wang J, Liu J, Khan K. Seismic behavior and moment transfer capacity of an innovative self-locking inter-module connection for modular steel building. Eng Struct 2021;245:112978. https://doi.org/10.1016/j.engstruct.2021.112978.

[51] Peng J, Hou C, Shen L. Numerical analysis of corner-supported composite modular buildings under wind actions. J Constr Steel Res 2021;187:106942. https://doi.org/10.1016/j.jcsr.2021.106942.

[52] Xu B, Xia J, Chang H, Ma R, Zhang L. Experimental and numerical investigation on the lateral force resistance of modular steel sub-frames with laminated double beam. J Build Eng 2022;46:103666. https://doi.org/10.1016/j.jobe.2021.103666.

[53] Lawson RM, Ogden RG, Bergin R. Application of Modular Construction in High-Rise Buildings. J Archit Eng 2012;18:148–54. https://doi.org/10.1061/(asce)ae.1943-5568.0000057.

[54] Alagha AN, Hussain S, Zaki W. Additive manufacturing of shape memory alloys: a review with emphasis on powder bed systems. Mater Des 2021;204:109654. https://doi.org/10.1016/j.matdes.2021.109654.

[55] Xue L, Atli KC, Zhang C, Hite N, Srivastava A, Leff AC, et al. Laser Powder Bed Fusion of Defect-Free NiTi Shape Memory Alloy Parts with Superior Tensile Superelasticity. Acta Mater 2022;229:117781. https://doi.org/10.1016/j.actamat.2022.117781.

[56] Lacey AW, Chen W, Hao H. Experimental methods for inter-module joints in modular building structures - a state-of-the-art review. J Build Eng 2022;46:103792. https://doi.org/10.1016/j.jobe.2021.103792.

[57] Dassault Systèmes SIMULIA Corp. Abaqus CAE 2019:2019.

[58] BSI. Structural bearings — part 3: elastomeric bearings. London: BSI; 2006.

[59] BSI. Anti-seismic devices. London: BSI; 2018.

[60] BSI. Eurocode 3: design of steel structures - part 1–1: general rules and rules for buildings. London: BSI; 2015.

[61] BSI. Execution of steel structures and aluminium structures - Part 2: technical requirements for steel structures. London: BSI; 2018.

[62] Gent AN. Engineering with rubber: how to design rubber components. 3rd ed. München: Hanser; 2012.

[63] Fang C, Wang W, He C, Chen Y. Self-centring behaviour of steel and steel-concrete composite connections equipped with NiTi SMA bolts. Eng Struct 2017;150:390–408. https://doi.org/10.1016/j.engstruct.2017.07.067.

[64] Fang C, Yam MCH, Lam ACC, Xie L. Cyclic performance of extended end-plate connections equipped with shape memory alloy bolts. J Constr Steel Res 2014;94:122–36. https://doi.org/10.1016/j.jcsr.2013.11.008.

[65] Speicher MS, DesRoches R, Leon RT. Experimental results of a NiTi shape memory alloy (SMA)-based recentering beam-column connection. Eng Struct 2011;33:2448–57. https://doi.org/10.1016/j.engstruct.2011.04.018.

[66] Orfeo A, Tubaldi E, Muhr AH, Losanno D. Mechanical behaviour of rubber bearings with low shape factor. Eng Struct 2022;266:114532. https://doi.org/10.1016/j.engstruct.2022.114532.

[67] Dassault Systèmes SIMULIA Corp. SIMULIA User Assistance 2020. Abaqus Theory; 2020.

[68] Yun X, Gardner L. Stress-strain curves for hot-rolled steels. J Constr Steel Res 2017;133:36–46. https://doi.org/10.1016/j.jcsr.2017.01.024.

[69] Bruneau M, Uang C-M, Sabelli R. Ductile design of steel structures. 2nd ed. London: McGraw Hill; 2011.

[70] Ramberg W, Osgood WR. Description of stress-strain curves by three parameters. Washington, D.C: National Advisory Committee for Aeronautics; 1943.

[71] Yeoh OH. Characterization of elastic properties of carbon-black-filled rubber vulcanizates. Rubber Chem Technol 1990;63:792–805. https://doi.org/10.5254/1.3538289.

[72] Yeoh OH. Some forms of the strain energy function for rubber. Rubber Chem Technol 1993;66:754–71. https://doi.org/10.5254/1.3538343.

[73] Bergstrom JS, Boyce MC. Constitutive modeling of the time-dependent and cyclic loading of elastomers and application to soft biological tissues. Mech Mater 2001; 33:523–30.
[74] Bergstrom JS. Mechanics of solid polymers : theory and computational modeling. 1st ed. London: Elsevier; 2015.
[75] PolymerFEM. MCalibration 2022.
[76] Lubliner J. A simple model of generalized plasticity. Int J Solids Struct 1991;28: 769–78. https://doi.org/10.1016/0020-7683(91)90155-9.
[77] Auricchio F, Taylor RL. Shape-memory alloys: modelling and numerical simulations of the finite-strain superelastic behavior. Comput Methods Appl Mech Eng 1997;143:175–94. https://doi.org/10.1016/S0045-7825(96)01147-4.
[78] Auricchio F, Taylor RL, Lubliner J. Shape-memory alloys: macromodelling and numerical simulations of the superelastic behavior. Comput Methods Appl Mech Eng 1997;146:281–312. https://doi.org/10.1016/S0045-7825(96)01232-7.
[79] Farmani MA, Ghassemieh M. Steel beam-to-column connections equipped with SMA tendons and energy dissipating devices including shear tabs or web hourglass pins. J Constr Steel Res 2017;135:30–48. https://doi.org/10.1016/j.jcsr.2017.04.003.
[80] Fang C, Yam MCH, Chan T-M, Wang W, Yang X, Lin X. A study of hybrid self-centring connections equipped with shape memory alloy washers and bolts. Eng Struct 2018;164:155–68. https://doi.org/10.1016/j.engstruct.2018.03.006.
[81] Wang B, Nishiyama M, Zhu S, Tani M, Jiang H. Development of novel self-centering steel coupling beams without beam elongation for earthquake resilience. Eng Struct 2021:232. https://doi.org/10.1016/j.engstruct.2020.111827.
[82] Nguyen HD, Choi E, Nguyen S-N, Pham T-K. Performance of self-centering devices containing superelastic SMA bars and their application via finite element analysis. Eng Struct 2021;237:112113. https://doi.org/10.1016/j.engstruct.2021.112113.
[83] Askariani SS, Garivani S, Hajirasouliha I, Soleimanian N. Innovative self-centering systems using shape memory alloy bolts and energy dissipating devices. J Constr Steel Res 2022;190:107127. https://doi.org/10.1016/j.jcsr.2021.107127.
[84] Qiu C, Liu J, Du X. Cyclic behavior of SMA slip friction damper. Eng Struct 2022; 250:113407. https://doi.org/10.1016/j.engstruct.2021.113407.
[85] Chen J, Wang W, Fang C. Manufacturing, testing and simulation of novel SMA-based variable friction dampers with enhanced deformability. J Build Eng 2022;45: 103513. https://doi.org/10.1016/j.jobe.2021.103513.
[86] Wang B, Jiang H, Wang J. Numerical simulation and behavior insights of steel columns with SMA bolts towards earthquake resilience. J Constr Steel Res 2019; 161:285–95. https://doi.org/10.1016/j.jcsr.2019.07.011.
[87] Yam MCH, Ke K, Huang Y, Zhou X, Liu Y. A study of hybrid self-centring beam-to-beam connections equipped with shape-memory-alloy-plates and washers. J Constr Steel Res 2022;198:107526. https://doi.org/10.1016/j.jcsr.2022.107526.
[88] Fang C, Zheng Y, Chen J, Yam MCH, Wang W. Superelastic NiTi SMA cables: thermal-mechanical behavior, hysteretic modelling and seismic application. Eng Struct 2019;183:533–49. https://doi.org/10.1016/j.engstruct.2019.01.049.
[89] Chen Z, Liu Y, Zhong X, Liu J. Rotational stiffness of inter-module connection in mid-rise modular steel buildings. Eng Struct 2019:196. https://doi.org/10.1016/j.engstruct.2019.06.009.
[90] Chen Z, Wang J, Liu J, Cong Z. Tensile and shear performance of rotary inter-module connection for modular steel buildings. J Constr Steel Res 2020:175. https://doi.org/10.1016/j.jcsr.2020.106367.
[91] Lacey AW, Chen W, Hao H, Bi K, Tallowin FJ. Shear behaviour of post-tensioned inter-module connection for modular steel buildings. J Constr Steel Res 2019:162. https://doi.org/10.1016/j.jcsr.2019.105707.
[92] Chen Z, Liu J, Yu Y, Zhou C, Yan R. Experimental study of an innovative modular steel building connection. J Constr Steel Res 2017;139:69–82. https://doi.org/10.1016/j.jcsr.2017.09.008.
[93] Rahnavard R, Thomas RJ. Numerical evaluation of steel-rubber isolator with single and multiple rubber cores. Eng Struct 2019:198. https://doi.org/10.1016/j.engstruct.2019.109532.
[94] Chopra AK. Dynamics of structures: theory and applications to earthquake engineering. 5th ed. Harlow: Pearson; 2020.